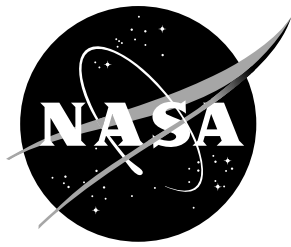NASA Technical Memorandum 112858

Comparative Results From a CFD Challenge Over a 2D Three-Element High-Lift Airfoil

Steven M. Klausmeyer
Wichita State University, Wichita, Kansas

John C. Lin
Langley Research Center, Hampton, Virginia

May 1997

Summary

A high-lift workshop was held in May of 1993 at NASA Langley Research Center. A major part of the workshop centered on a blind test of various computational fluid dynamics (CFD) methods in which the flow about a two-dimensional (2D) three-element airfoil was computed without prior knowledge of the experimental data. Comparisons were made between computation and experiment for (a) lift, drag, and moment, (b) lift and drag increments due to Reynolds number and flap gap changes, (c) pressure and skin-friction distributions, and (d) mean velocity profiles.

The results of this 'blind' test revealed:
1. There was good agreement between several codes and the experimental results. In general, the Reynolds Averaged Navier-Stokes (RANS) methods showed less variability among codes than did potential/Euler solvers coupled with boundary-layer solution techniques. However, some of the coupled methods still provided excellent predictions.
2. Drag prediction using coupled methods agreed more closely with experiment than the RANS methods. Lift was more accurately predicted than drag for both methods.
3. The CFD methods did well in predicting lift and drag changes due to changes in Reynolds number, however, they did not perform as well when predicting lift and drag increments due to changing flap gap.
4. Pressures and skin friction compared favorably with experiment for most of the codes.
5. There was a large variability in most of the velocity profile predictions. Computational results predict a stronger slat wake than measured suggesting a missing component in turbulence modeling, perhaps curvature effects.

Symbols

c	= cruise or stowed airfoil chord
C_D	= drag coefficient
C_f	= skin-friction coefficient, where $C_f = \tau_{wall}/q_\infty$
C_L	= lift coefficient
C_p	= pressure coefficient
M_∞	= freestream Mach number
n	= distance normal to airfoil surface
q_∞	= freestream dynamic pressure

Re	= Reynolds number based on cruise chord c
x	= coordinates along the chord direction
α	= angle of attack
Δ	= differential value
τ_{wall}	= wall shear stress
Subscripts	
max	= maximum value

Introduction

A High-Lift Workshop/CFD Challenge was held at NASA Langley Research Center in May of 1993. The primary objectives of the workshop were to define the state-of-the-art in 2D multi-element airfoil prediction techniques, to determine the status of high-lift research in the U.S., and to discuss high-lift flow physics. Conference participants included NASA and industry.

The main thrust of the workshop centered on a comparison of several sets of computational results with 2D experimental data at Reynolds numbers of 5 and 9 million. A total of 15 sets of computational results were submitted in the challenge. All computations were performed without prior knowledge of the experimental results and each challenge participant received the experimental data only after sending his/her calculations to Langley.

Experiment

The experiment is described in detail by Chin et. al. (Reference 1). A brief description is repeated below.

The experimental data set was obtained in the Low-Turbulence Pressure Tunnel (LTPT) at NASA Langley Research Center in a cooperative effort with McDonnell Douglas Aerospace West. The data includes force and moment data, pressure and skin-friction distributions, and mean velocity profiles.

Integration of the chordwise pressure measurements yielded the lift data, while integration of the downstream wake profile yielded the drag data. The skin friction data were obtained using 0.020 inch diameter Preston tubes. Using the Kline and McClintock method, the uncertainty in $C_{L, max}$ was calculated to be approximately ±0.02 (or less than 1% for a $C_{L, max}$ value of 4.5), while the uncertainty in C_D was calculated to be approximately ±0.0010 for high-lift models (e.g., 2.5% for a typical C_D value of 0.0400).[2] Repeatability studies confirmed these levels. The maximum error in C_f was calculated to be less than 6%.[3]

The high-lift model investigated is a McDonnell Douglas Aerospace (MDA) 2D, single-flap, three-element airfoil as shown in Figure 1(a). The 11.55% thick super critical airfoil model spanned the width of the test section (36 inches) and had a reference (stowed) airfoil chord, c, of 22 inches. The slat chord is 14.48% and the flap chord is 30% of the stowed airfoil chord. The airfoil was configured in a typical approach/landing configuration with slat and flap deflections of 30°. Two different flap riggings were used in the test as shown in Table 1. Figure 1(b) defines the nomenclature for gap and overhang. The first flap rigging was designated as 30P/30N by MDA and Geometry A for the workshop. The second flap rigging had a larger gap and was designated 30P/30AD (Geometry B).

Computed Results and Comparison to Experiment

Two types of computational techniques were used in the CFD Challenge: 1) Reynolds Averaged Navier-Stokes (RANS) methods and 2) Potential/Euler methods coupled with integral boundary-layer techniques. Several turbulence models were represented in the RANS solutions.

Both structured and unstructured grids were used in the solutions. The structured grids were of the Chimera and block types while the unstructured grids were composed of triangular elements.

Challenge participants are listed in Table 2 along with code name, legend key, solution scheme, grid type, and turbulence model.

The challenge consisted of five computational cases that are list in Table 3. The first three cases were mandatory for each participant and the last two were optional. These cases represent four different classes of flow conditions for a high-lift system: 1) attached flow

(Cases 1, 2, and 4); 2) Flap separation at low angle of attack (Cases 1 and 4); 3) $C_{L,max}$ (Case 3); and 4) Stall (Case 5).

Comparison of Computed and Experimental Data

This section contains the computational results of each high-lift challenge participant plotted against the experimental data. To facilitate comparison between calculation and experiment, the computational results were split into two basic categories according to solution technique: 1) methods in which an Euler or potential solver was coupled to a boundary-layer scheme and 2) Reynolds Averaged Navier-Stokes methods.

Force and Moment Predictions

Geometry A - Re=5,000,000

Computed lift, drag and pitching moment coefficients are plotted against experiment for Geometry A at a Reynolds number of 5 million in Figure 2. Calculations were performed at α's of 8°, 16°, and 21°. Coupled method solutions are shown in Figure 2(a) and RANS methods are plotted in Figure 2(b). The experimental values are the same in the upper and lower graphs.

This configuration has flow separation near the flap trailing edge around α=8° and the flow reattaches near α=12°. The experimental lift curve is nearly linear up to α=14° except for a small dip near α=8° where the flap separated. This depression in the lift curve corresponds to a significant drag increase indicated by the peak in the drag polar near C_L=3.1. Above α=14°, the lift curve slope suddenly decreases, possibly due to boundary-layer confluence. $C_{L,max}$ occurred near α=21° and was followed by a gradual lift drop-off indicating a fairly mild stall. Drag was not measured above α=16°, however, a rapid increase near $C_{L,max}$ would be expected.

Some of the lift calculations agree quite well with the experiment, but in general the solutions indicate a higher C_L. There is a fairly large variation in lift prediction between the

codes and the variation appears larger for the coupled methods than for the RANS methods.

Drag calculations by the coupled method solutions agreed with experiment much more closely than the RANS methods and also showed lower variability between codes. In general, calculations indicate a higher drag than shown experimentally, particularly for the RANS methods. Drag calculations by RANS methods are usually very sensitive to the proximity of the outer boundary to the airfoil and to the outer-boundary conditions, particularly at large lifts. The outer boundary can influence the force vector angle and a small angle change can lead to very large drag changes. The effect of outer-boundary conditions can be seen in the solutions labeled 'kyle' and 'kyleff'. Much closer agreement with experiment was obtained by modeling the effect of airfoil circulation on the outer boundary using the point-vortex method ('kyleff'). The coupled methods (except the 'drela' calculations) are not effected by outer boundary conditions which may have reduced variation in drag predictions.

Pitching moment was computed with reference to the 25% chord location with negative values indicating a nose down moment. Experimental results show a reduction in nose down moment as angle of attack increased. This was caused by the large increases in suction on the slat and main-element leading edge and a relatively constant suction level on the flap. Predictions from the couple methods showed a larger variation among codes than the RANS codes, similar to the lift case.

Geometry A - Re=9,000,000 (Increased Reynolds Number)

Computed force and moment coefficients for Geometry A at a larger Reynolds number of 9 million are shown in Figure 3 along with the experimental data. In this case the flap remained attached at the lower α's, thus the lift loss near $\alpha=8°$ and the drag increase near $C_L=3.1$ for the Re=5,000,000 case are not present. The lift curve remains relatively linear up to about $\alpha=12°$ followed by a gradual rounding. $C_{L,max}$ occurs near $\alpha=21°$ followed by a mild stall.

The calculated results show similar trends as in the Re=5,000,000 case. Computed lift was higher than that shown experimentally. Variation in lift calculation for the coupled methods was greater than that of the RANS methods. Drag levels at low angles of attack were better

predicted by the coupled methods. In general, there was a large discrepancy between calculated drag and the experiment. Pitching moment prediction by the coupled methods had more variation than for the RANS methods.

Geometry B - Re=9,000,000 (Flap Gap Increase)

Geometry B represents an increase in flap gap of 0.23% chord. Increasing the gap produced a large separation region on the flap around $\alpha=16°$ causing a lift loss, a sudden large drag increase, and a decrease in nose down pitching moment.

The calculations for this case (Figure4) show similar trends in lift and pitching moment predictions but are in much better agreement with the experimental drag than in the previous two cases (Geometry A, Re=5, 9 million). Interestingly, the computed drag values have not changed significantly from the previous two cases, however, the experimentally measured drag increased, narrowing the gap between the computed and experimental values.

Geometry B - Re=9,000,000 (Detailed Lift/Drag/Moment)

In the previous three cases, calculations were performed at only three angles of attack ($\alpha=8°$, 16°, and 21°). A more detailed prediction of the lift curves, drag polar, and pitching moment curves are shown in Figure 5 along with the experimental data. The calculations were conducted with a much closer angle-of-attack increment ($\alpha=4°$, 8°, 12°, 14°, 16°, 19°, 21°, 22°, and 23°). Very few of the codes predicted a lift break-off at $C_{L,max}$ or the lift decrease near $\alpha=16°$ due to flap separation. The drag increase near $C_L=3.8$ also was not predicted. These results seem to indicate an inability of the codes to predict flow separation.

Increments in Lift and Drag

One of the primary benefits of using computational methods in developing high-lift multi-element airfoils is to get some idea of the effects of changing gap/overhang between the various elements and to determine the effects of Reynolds number on airfoil performance. Determining gap/overhang effects can significantly reduce configuration optimization time

in the wind tunnel by narrowing the element position matrix, thus saving time and money. Determining Reynolds number effects is necessary for prediction of the airfoil performance at flight Reynolds numbers.

When calculating lift and drag changes it is very important to predict the sign and magnitude of the change correctly. The sign is critical because it determines whether a change improves or degrades airfoil performance which drives the optimization process. The magnitude is important because it determines the amount of performance improvement or degradation associated with a given change.

Geometry Changes

The experimentally measured lift and drag increments due to increasing flap gap at Re=9,000,000 are shown in Figure 6. Flap separation at intermediate angles of attack caused a lift decrease, however, lift increased at low and high angles of attack where the flow remained attached. Drag increased across the angle-of-attack range, especially at α's where the flap separated.

Computed lift increments due to an increase in flap gap are given in Figure 7. At $\alpha=8°$, all the coupled methods predict a lift loss which agrees with experiment, however, the magnitude of the change is quite different, with the experimental value hovering near the zero-increment line and the computed values ranging from -0.02 to -0.07. Six of the RANS solutions also gave a lift decrease, however, four predicted a lift increase. The coupled methods have less scatter at the low angle of attack than the RANS methods.

Drag increments due to flap gap change are shown in Figure 8. The experiment indicated a drag increase, however, the computed results are scattered about the zero-increment line.

Reynolds Number Change

Lift and drag increments for Geometry A due to increasing Reynolds number are shown in Figure 9. Recall that the flap separated at lower α's for the Re=5,000,000 condition. Increasing Reynolds number eliminated the flap separation as indicated by the local peak in ΔC_L and the dip in ΔC_D at $\alpha=8°$ in Figure 9. A large increase in lift was also observed

above $\alpha=15°$ with most of the increase coming from the main element. The wake width from the main element was smaller at the higher Reynolds number, which may have allowed a slightly larger suction on the flap which caused a higher loading on the main element.

Computed increments in lift and drag are shown in Figures 10 and 11 along with experimental values at 8° and 16°. In general, the computed ΔC_L was lower than the experimental value. However, most of the calculations fall within the ±0.04 to ±0.06 variation in the experimental data.

A decrease in drag with increasing Reynolds number was predicted by nearly all of the codes.   At $\alpha=8°$, the computed drag decrease was smaller than that observed experimentally. The experimental value was large due to reduction of flap separation at higher Reynolds number. The codes may not have predicted flap separation at the lower Reynolds number, thus missing this effect.   The codes predicted an increase in drag reduction (ΔC_D more negative) as angle of attack increased.   Experimental data is not available past 15°, however, the trends seem to indicate that ΔC_D becomes slightly more positive with increasing angle of attack.

Pressure Distributions

Computed pressure distributions for $\alpha=8.12°$ and 21.29° at a Reynolds number of 5 million are used for comparison with experiment.

Pressure Distributions at $\alpha=8°$

Computed and experimental pressure distributions for the slat, main element, and flap for the low α (8°) flap separation case are shown in Figures 12, 13, and 14, respectively. In general, computed suction on the upper surface of the slat (Figure 12) was higher than the experimental values except for three codes which closely agreed with the experimental values. The slat produces a thrust force since the it is deflected downward and the suction surface faces forward. Note that the 'kyleff' solution shows a larger upper surface suction

than the 'kyle' solution. This difference was largely responsible for the drag differences in Figure 1. Interestingly, the higher suction levels predicted by the codes suggests that the computed drags would be less than experiment, not more. However, higher computed suction levels on the flap pull in the opposite direction, partially canceling the slat contribution.

In general, the coupled methods showed more scatter between codes than the RANS methods. The RANS methods also predicted the lower surface/cove pressures more accurately.

The main-element pressure distribution shown in Figure 13 is typical of multi-element airfoils with a large suction peak near the leading edge followed by a pressure recovery region and then leveling off into a flat suction plateau. Note that pressure does not recover back to freestream levels since the trailing edge is adjacent to the flap suction peak. The under surface is characterized by high pressure, nearly stagnating flow (C_P near 1). Computed upper surface suction was generally higher than the experiment except near the leading edge where calculations were scattered above and below the experimental results.

The stagnation location greatly effects the suction peak. This can be seen in the slat pressure distributions where the solutions with the higher suction peaks have a more rearward stagnation point. Small errors in stagnation point prediction can lead to large suction differences, suggesting that grid clustering around the stagnation point is important.

Separation on the flap is observed in Figure 14 as a slight flattening of the experimental pressure distribution near the trailing edge. A few of the codes predicted a flattening of the pressure distribution typical of separation. Nearly all the codes predicted a higher suction level on the upper flap surface than that found experimentally.

Pressure Distributions at α=21.29°

Pressure distributions on the slat, main element, and flap near $C_{L,max}$ (α=21.29°) are shown in Figures 15, 16, and 17, respectively.

Note the very large suction peak on the slat (C_P=-17 experimentally) shown in Figure 15. For a freestream Mach number (M_∞) of 0.2, the critical C_P is -16.3, thus there is a small

region of supersonic flow near the slat leading edge. Computed pressures on the slat indicate a higher suction peak than the experiment which would result in a higher Mach number region and a stronger shock. The coupled method solutions exhibit more variability than the RANS methods.

The main-element pressures shown in Figure 16 show similar trends as the $\alpha=8.12°$ case.

Suction levels on the flap upper surface (Figure17) did not change significantly from the $\alpha=8.12°$ case. Since the flap is located in the downwash from the main element, its local angle of attack stays nearly constant throughout the angle-of-attack range, thus the pressures remain fairly constant. Experimental boundary-layer measurements indicated that the flap was not separated at this angle of attack even though the upper surface pressure distribution shows a separation-like flattening on the aft 50%. Several of the coupled methods predicted flap separation as will be seen in the discussion of skin-friction results.

Skin Friction

Computed skin-friction distributions for $\alpha=8.12°$ and $21.29°$ at a Reynolds number of 5 million were chosen for comparison to experiment.

Skin Friction at $\alpha=8°$

Computed and experimental skin-friction distributions for the slat, main element, and flap for the low angle of attack ($\alpha=8°$) flap separation case are shown in Figures 18, 19, and 20, respectively.

Computed skin-friction data for the slat (upper surface only) is shown in Figure 18. Experimental data is not available, since the upper surface boundary layer was nearly all laminar and the Preston tube skin-friction measurement technique is valid only for turbulent boundary layers. The calculations show a wide range of skin-friction levels due to widely varying transition locations. The RANS solutions are split between two distinct skin-friction-coefficient (C_f) levels, one around $C_f=0.01$ (transition near leading edge) and the other around $C_f=0.003$ (transition near trailing edge). Transition is indicated by an increase in skin friction preceded by a low skin-friction level.

Skin-friction behavior on the main-element upper surface (Figure 19) is typical of a single-element airfoil characterized by large C_f values near the leading edge (due to high velocity flow and thin boundary layers) which decrease downstream (due to slowing flow and thicker boundary layers). The large skin-friction value at the trailing edge of the main element is somewhat different from single-element airfoils which typically show a drop in C_f near the trailing edge due to the adverse pressure gradient. This occurs since the trailing edge of the main element is located near the flap suction peak which keeps trailing edge velocities large and prevents a drop-off in C_f. The coupled method predictions show a large amount of scatter between codes, possibly due to the various integral boundary-layer methods. The RANS methods showed much less variability. For most of the codes, there is good agreement with the experiment.

Boundary-layer separation on the flap is indicated in Figure 20 as the C_f values approach zero near the trailing edge. Separation location was estimated from the experimental data at about x/c=1.06. Computed separation location varied widely among the codes. The large dips in C_f near x/c=0.92 are the boundary-layer transition locations. Changing the flap transition location had a large effect on the separation location between the 'amir' and 'amirt' solutions. Separation location moved from 1.07 to 1.10. This seems plausible since the earlier transition causes a larger energy loss in the boundary layer. Calculated skin friction on the flap shows more variation between codes than for the main element possibly due to the influence of the boundary-layer confluence on the flap.

Skin Friction at α=21°

Skin-friction distributions for the slat, main element, and flap near $C_{L,max}$ (α=21.29°) are shown in Figures 21, 22, and, 23, respectively. The coupled-method solutions appear to have less variability than the RANS methods.

The slat skin-friction distribution (upper surface only) is shown in Figure 21. A few solutions showed a separation bubble near the slat leading edge (x/c=-0.085) which was possibly induced by a shock. In general there was a very large variability between the solutions.

As seen in Figure 22, C_f behavior on the main element is similar to the previous case although skin friction is slightly higher than the $\alpha=8°$ case near the leading edge and slightly lower near the trailing edge. The higher values near the leading edge are probably caused by the highly accelerated flow and the lower values near the trailing edge are possibly due to the larger adverse pressure gradient.

Experimental skin-friction values for the flap indicate that the flow has reattached at this angle of attack (Figure 23). A few of the coupled methods predicted flow separation near the trailing edge.

Velocity Profiles

Velocity profiles were measured at nine locations on the upper surfaces of the main element and flap for Geometries A and B. The profiles were obtained using a flattened total pressure tube and a five-hole probe which were traversed normal to the airfoil surface. Comparisons to computed results are presented for one location on the main element and three locations on the flap for **Geometry A** only.

Velocity Profiles at $\alpha=8.12°$

Velocity profiles near the mid-chord of the main element are shown in Figure 24. According to the experimental data, the main-element boundary-layer edge is just below $n/c=0.01$. The slat wake passes just above the boundary layer and shows very little velocity deficit. Most of the codes predicted a slightly thicker boundary layer than found experimentally, this is possibly due to artificial dissipation effects of the RANS methods or a transition location too far forward. Interestingly, many of the codes predicted a larger velocity deficit in the slat wake which indicates that the turbulence models may be missing a key part of the physics. The rapid diffusion of the slat wake may be due to large streamline curvature effects near the main-element leading edge, however most eddy viscosity models do not include curvature effects. Another hypothesis is that turbulence production in the slat cove region may effect the slat wake diffusion.

Velocity profiles on the flap near the leading edge are presented in Figure 25. The profile in this region usually consists of four levels. Going from the surface outward these four levels are: 1) flap boundary layer, 2) slot flow through the flap gap, 3) main element

wake, and 4) slat wake. The flap boundary layer is extremely thin at this location, thus experimental data could not be taken in this region. Experimentally, the slot flow extends from 0.001<n/c<0.01 and is ramp shaped indicating strong viscous effects on the slot flow coming through the flap gap. These viscous effects are quite possibly generated by the separated and recirculating flow in the flap cove. The main-element wake extends from n/c=0.01 to n/c=0.025 and is very asymmetric, which is a challenging situation for eddy-viscosity turbulence models. The calculations show good general agreement with experiment, however, a few solutions show a large slat wake deficit that did not appear in the experiment.

At the flap mid-chord (Figure 26), the boundary layer is much thicker, and the main-element wake is more symmetric and is beginning to merge with the boundary layer. There are some good agreements between experiment and computed main-element wake location (e.g., "kyle" and "kyleff"). Variation in the amount of wake deficit prediction is large. A few of the codes predict a notable slat wake defect also.

Flow separation near the flap trailing edge is indicated by both the experiment and the calculations in Figure27. Since the experimental data was obtained using a total pressure tube, reverse velocities could not be measured. Nevertheless, when the data approaches zero and becomes quite variable, intermittent separation is indicated. Most of the calculations also showed a small amount of separation at this location.

Velocity profiles at α=21.29°

The mid-chord main-element velocity profile near $C_{L,max}$ is shown in Figure 28. At this angle of attack, the slat is highly loaded resulting in a strong slat wake at this location. The slat wake deficit showed better agreement between calculation and experiment for this condition, however the width and height of slat wake was over predicated.

Profiles at the leading edge and mid-chord of the flap are shown in Figures 29 and 30. There is considerably more scattering in the predictions for the flap than those for the main element, especially at the mid-chord section of the flap.

Velocity profiles near the flap trailing edge (Figure 31) show a very large main-element wake. In fact the experimental profile contains significant scatter and very low velocities indicating intermittent flow reversal in the wake.

Summary of Results

A workshop on 2D high-lift multi-element airfoils was held in May of 1993 at NASA Langley Research Center. The primary focus of this workshop was to determine the state-of-the-art in computational techniques, to discuss industry needs and high-lift flow physics issues.

A major part of the workshop centered on a blind test of various computational methods in which the flow about a three-element airfoil was computed without prior knowledge of the experimental data. Comparisons were made between computation and experiment for

- lift, drag, and moment

- lift and drag increments due to Reynolds number and flap gap changes

- pressure and skin-friction distributions

- mean velocity profiles

The results of this 'blind' test revealed:

1. There was good agreement between several codes and the experimental results. In general, the Reynolds Averaged Navier-Stokes methods showed less variability than did potential/Euler solvers coupled with boundary-layer solution techniques. However, some of the coupled methods still provided excellent predictions.

2. Coupled-methods drag prediction agreed more closely with experiment than the RANS methods. Lift was more accurately predicted than drag for both methods.

3. The codes did reasonably well in predicting lift and drag changes due to changes in Reynolds number, although they all missed the drag rise caused by a mild flow separation on the flap at low Reynolds number. The codes also did not perform as well when predicting lift and drag increments due to changing flap gap.

4. Pressures and skin friction compared favorably with experiment for most of the codes.

5. There was a large variability in most of the velocity profile predictions. Computational results predict a stronger slat wake than measured, suggesting a missing component in turbulence modeling, perhaps curvature effects.

Several flow-physics issues were discussed during the workshop. The need for accurate transition locations was emphasized since this appears to have a major influence on overall airfoil performance. Transition on the slat upper surface is thought to have a major effect on $C_{L,max}$ performance since it controls the size of the slat wake, which in turn influences $C_{L,max}$.

Three-dimensional testing is really the key item of concern, so more three-dimensional data is desirable.

The effects of turbulence generation in the slat and main-element coves is virtually unknown.

References

1. Chin, V.D.; Peters, D.W.; Spaid, F.W.; and McGhee, R.J.: Flowfield Measurements about Multi-Element Airfoil at High Reynolds Numbers. AIAA Paper 93-3137, AIAA 24th Fluid Dynamics Conference, July, 1993.

2. Lin, J. C.; Robinson, S. K.; McGhee, R. J.; and Valarezo, W. O.: Separation Control on High-Lift Airfoils Via Micro-Vortex Generators. *J. Aircr.*, vol. 31, no. 6, Nov.-Dec. 1994, pp. 1317-1323.

3. Klausmeyer, S. M.; and Lin, J. C.: An Experimental Investigation of Skin Friction on a Multi-Element Airfoil. AIAA Paper 94-1870, 12th AIAA Applied Aerodynamics Conference, June 1994.

Table 1. Slat and Flap Setting

	Geometry A (30P-30N)	Geometry B (30P-30AD)
Slat Deflection (δ_s)	-30°	-30°
Slat Gap, %c	2.95	2.95
Slat Overhang, %c	-2.5	-2.5
Flap Deflection (δ_f)	30°	30°
Flap Gap, %c	1.27	1.5
Flap Overhang, %c	0.25	0.25

Table 2. CFD Challenge Participants Summary

Legend Key	Person	Affiliation	Program	Type	Grid	Modeling Notes
Kyle	Anderson/ Bonhaus	Langley	FUN2D	RANS	Unstructured	Without point vortex farfield corrections
Kyleff	Anderson/ Bonhaus	Langley	FUN2D	RANS	Unstructured	With point vortex farfield corrections
jones	Jones	Langley	CFL3D	RANS	Structured-Chimera	
bied	Biedron	Langley	CFL3D	RANS	Structured-Eiseman multi-block	
vatsa	Vatsa	Langley	TLNS3D	RANS	Structured-Eiseman multi-block	
dod	Dodbele	Langley	MCARF	Coupled	-	
mavk	Mavriplis/ Klausmeyer	Langley	NSU2D	RANS	Unstructured	
stusb	Rogers	Ames	INS2D	RANS	Structured-Chimera	Baldwin/Barth turbulence model
stusa	Rogers	Ames	INS2D	RANS	Structured-Chimera	Spalart/Allmaras turbulence model
stuso	Rogers	Ames	INS2D	RANS	Structured-Chimera	k-ω turbulence model
drela	Drela	MIT	MSES	Coupled	Structured	
hawk	Hinson/ Hawke	Learjet	MEAFOIL	Coupled	-	
wood	Woodson	Cessna	MCARF	Coupled	-	
caobb	Cao/ Kusunose	Boeing	INS2D	RANS	Structured	Baldwin/Barth turbulence model
caoba	Cao/ Kusunose	Boeing	INS2D	RANS	Structured	Spalart/Allmaras turbulence model
amir	Amirchoupani	Boeing		Coupled	-	Free transition
amirt	Amirchoupani	Boeing		Coupled	-	Fixed transition

Table 3. Case Summary

Case	Geometry	Angle of Attack	Reynolds Number	Comments
1	A (30P-30N) A B (30P-30AD)	8.12° 8.10° 8.10°	5 million 9 million 9 million	flap separation flap separation
2	A A B	16.21° 16.21° 16.24°	5 million 9 million 9 million	
3	A A B	21.29° 21.34° 21.31°	5 million 9 million 9 million	$C_{L,max}$ $C_{L,max}$ $C_{L,max}$
4*	B	4.07° to 23.34°	9 million	flap separation between 8° to 14°
5*	A B	23.28° 23.34°	9 million 9 million	Stall Stall

* Optional
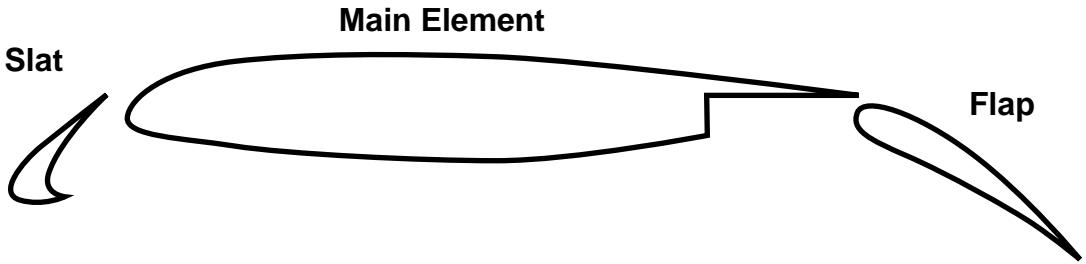
(a) McDonnell Douglas Aerospace three-element airfoil
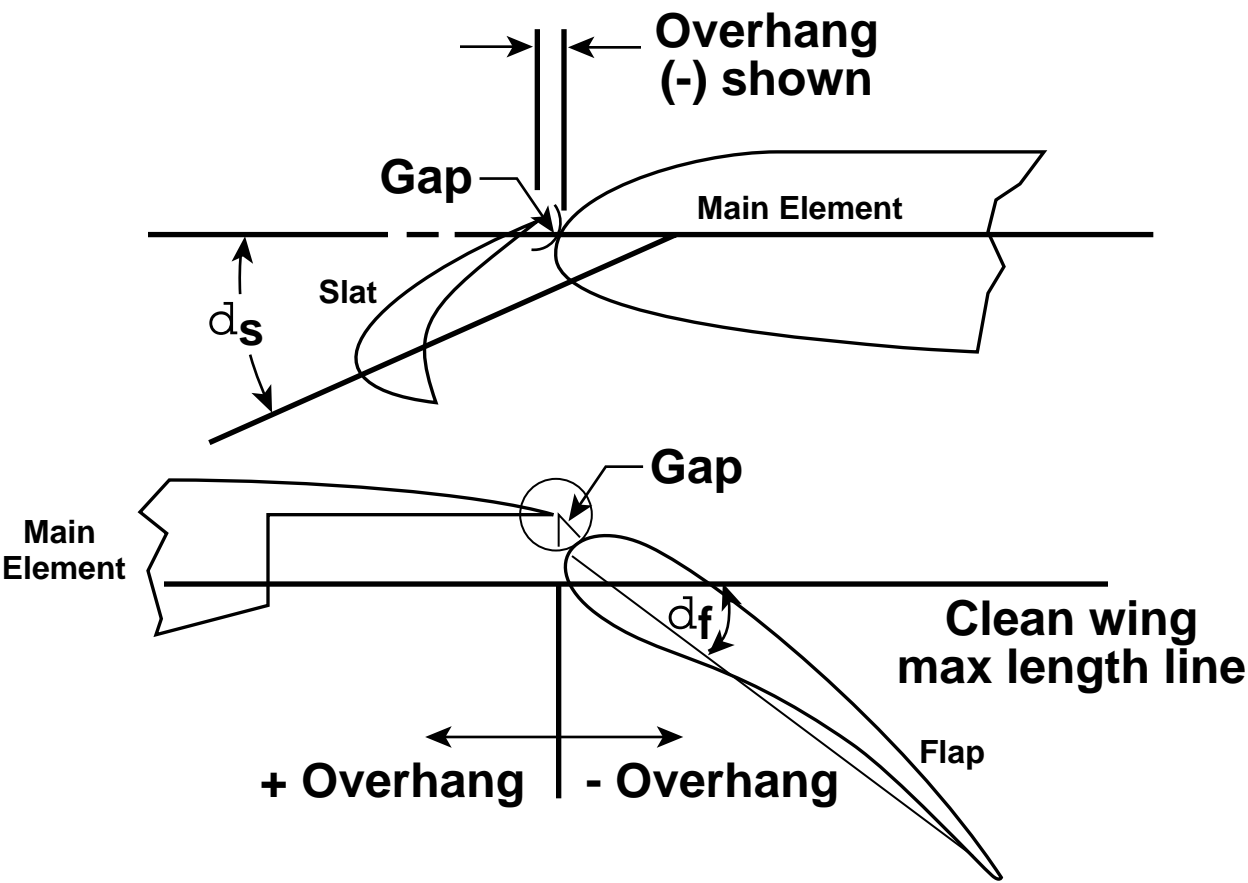
(b) Nomenclature for multi-element airfoil

Figure 1. Model geometry and nomenclature

(a) Coupled Methods
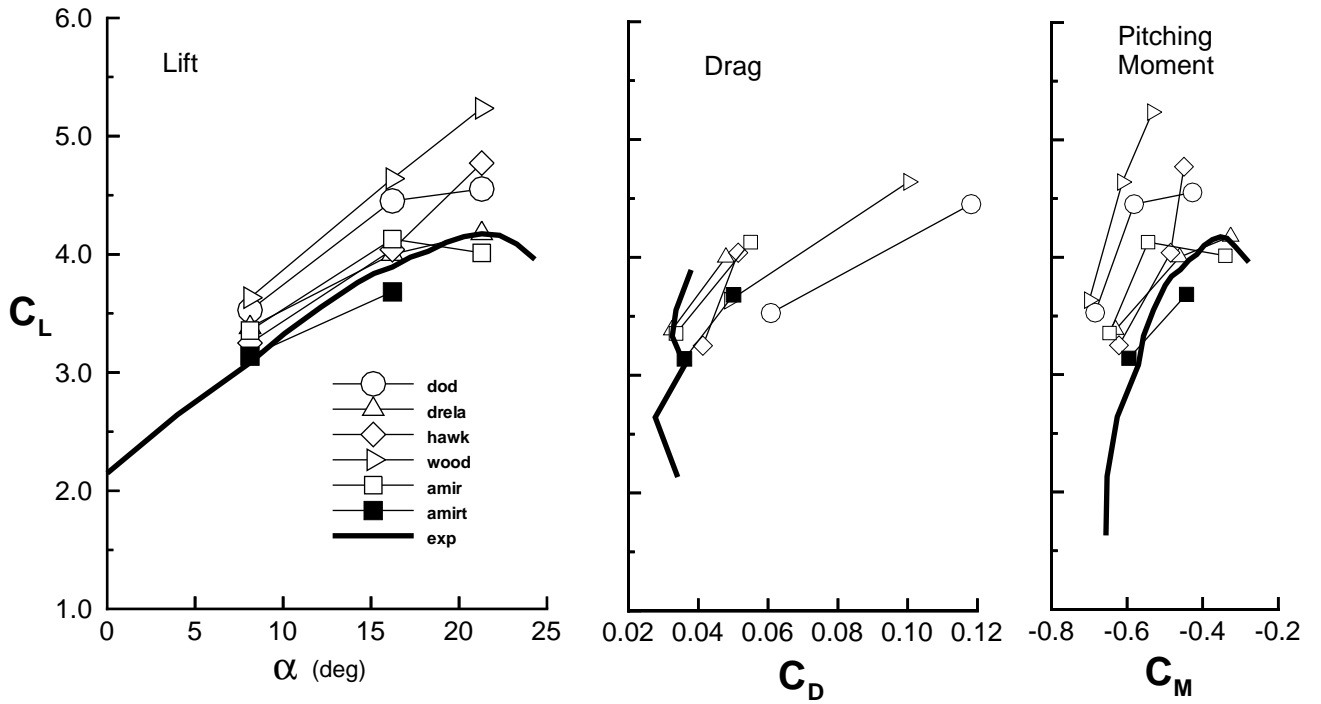
(b) Reynolds Averaged Navier-Stokes Methods
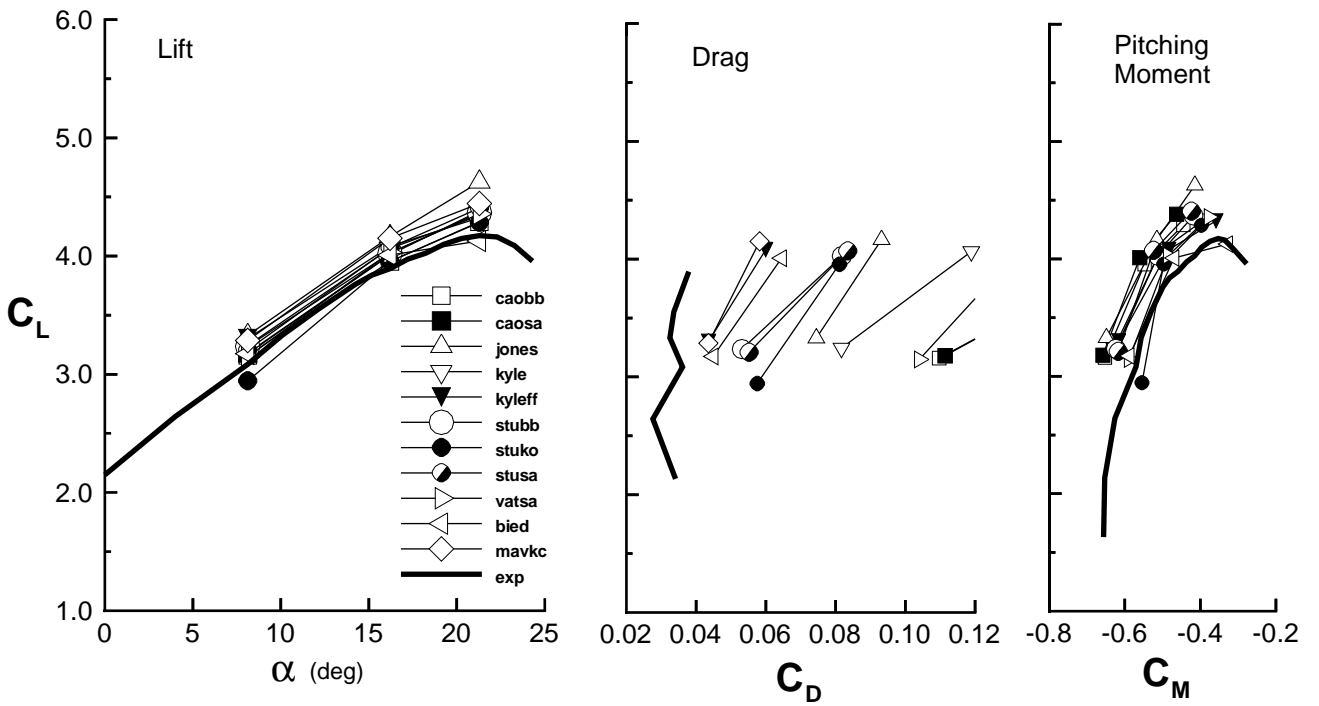
Figure 2. Force and moment coefficients for Geometry A, Re=5,000,000

20

(a) Coupled Methods

Lift

Drag

Pitching Moment

Legend:
- ○ dod
- △ drela
- ◇ hawk
- ▷ wood
- □ amir
- ■ amirt
- — exp

(b) Reynolds Averaged Navier-Stokes Methods

Lift

Drag

Pitching Moment

Legend:
- □ caobb
- ■ caosa
- △ jones
- ▽ kyle
- ▼ kyleff
- ○ stubb
- ● stuko
- ◑ stusa
- ▷ vatsa
- ◁ bied
- ◇ mavkc
- — exp
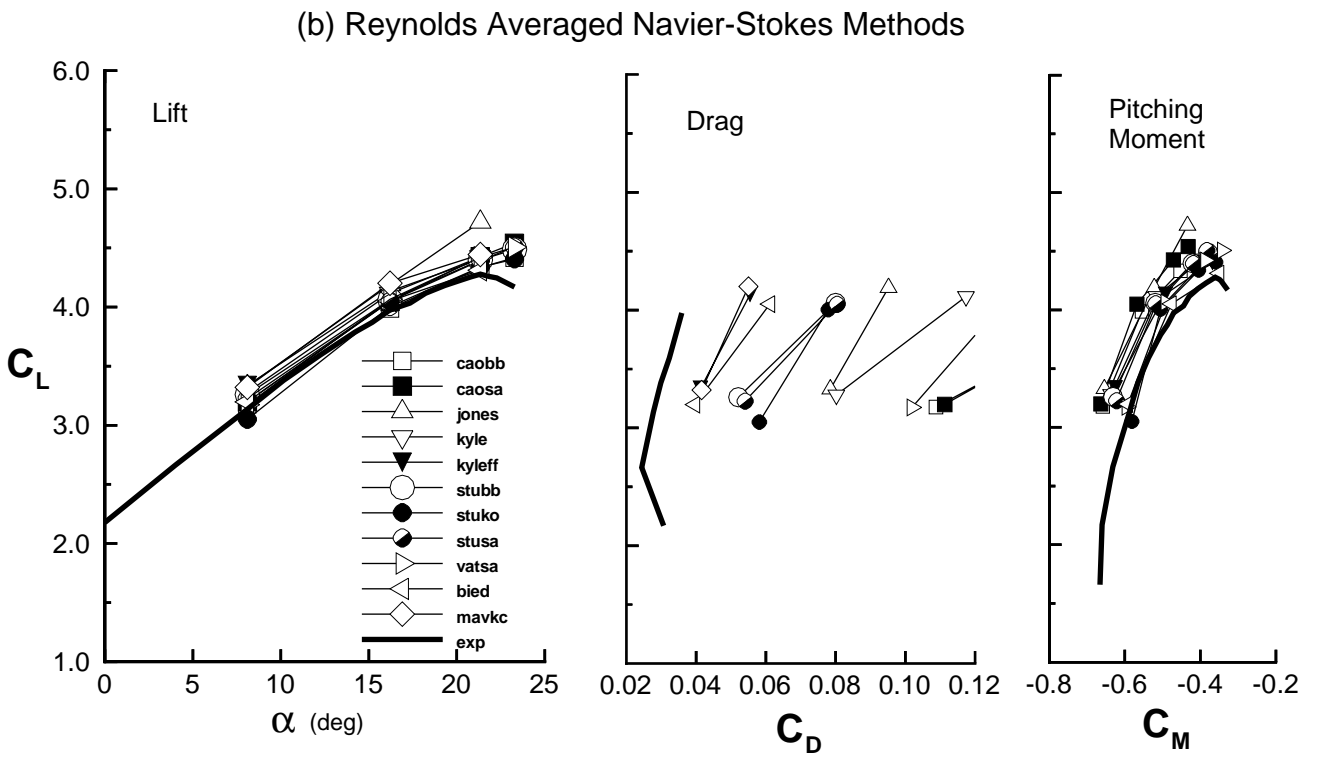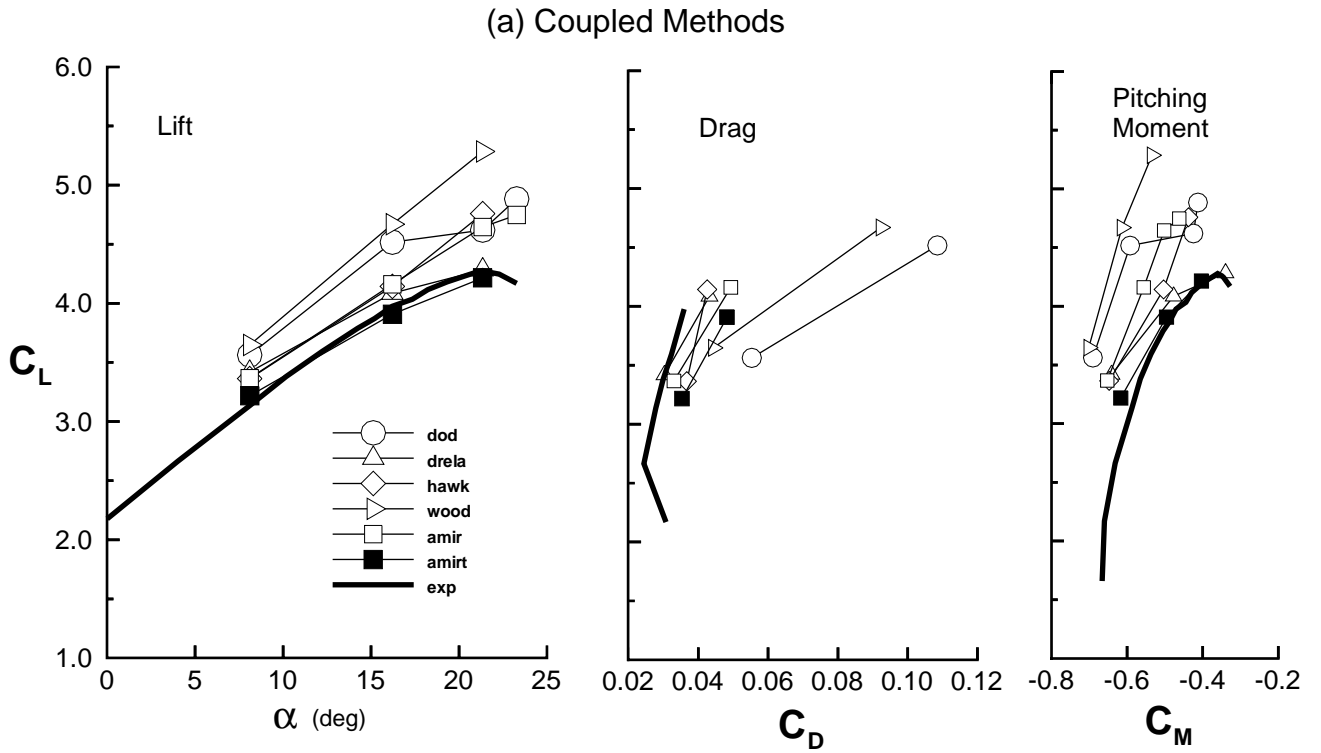
Figure 3. Force and moment coefficients for Geometry A, Re=9,000,000

21
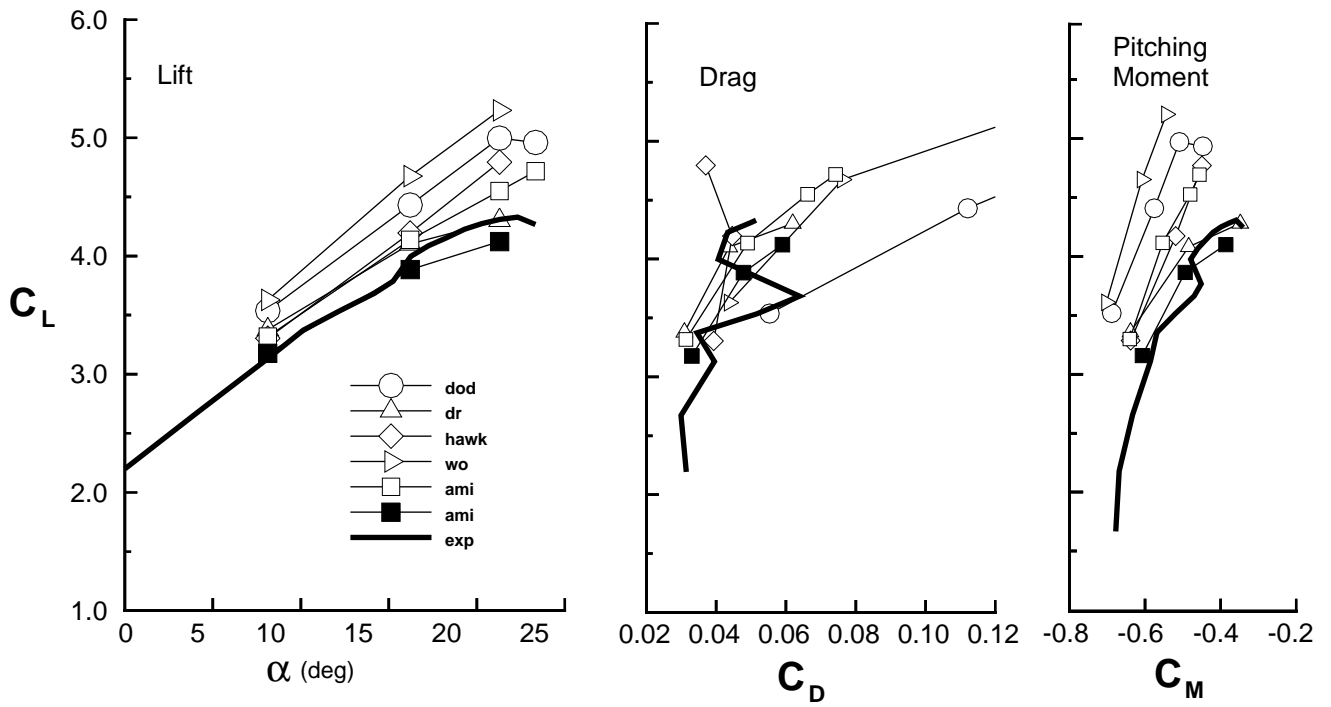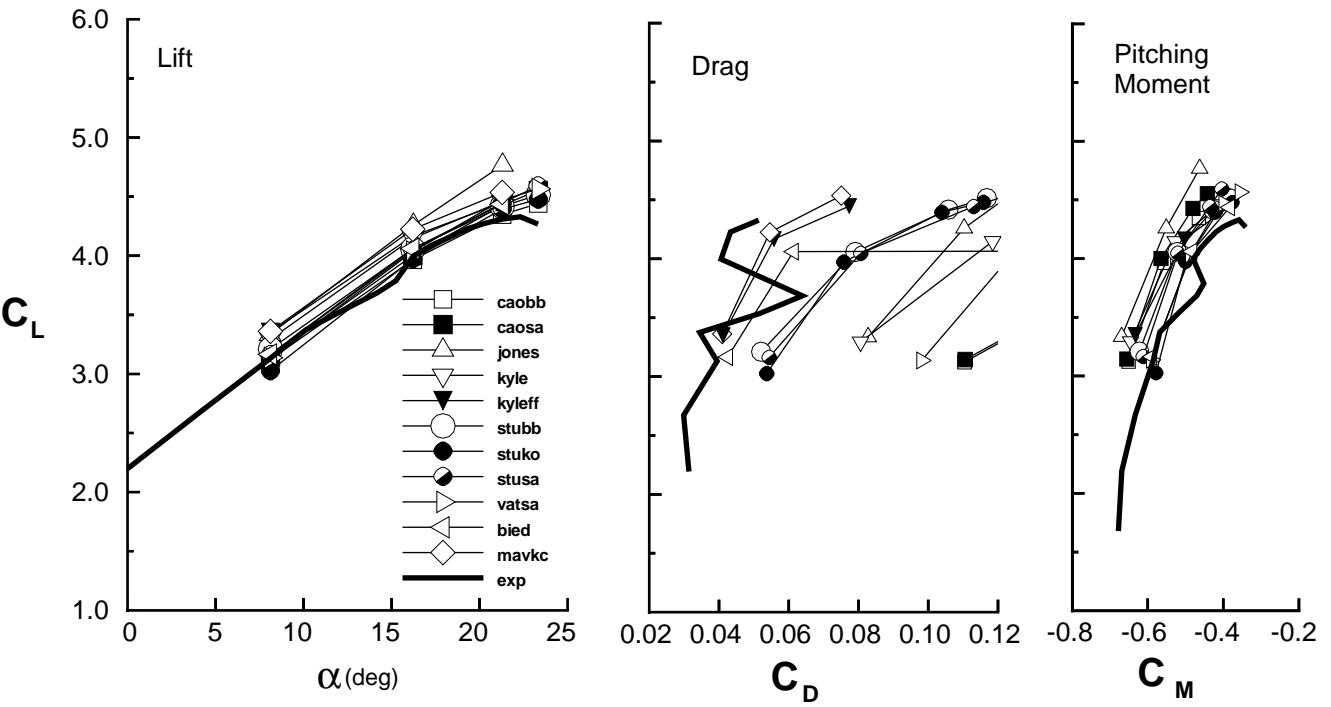
Figure 4.   Force and moment coefficients for Geometry B, Re=9,000,000

22
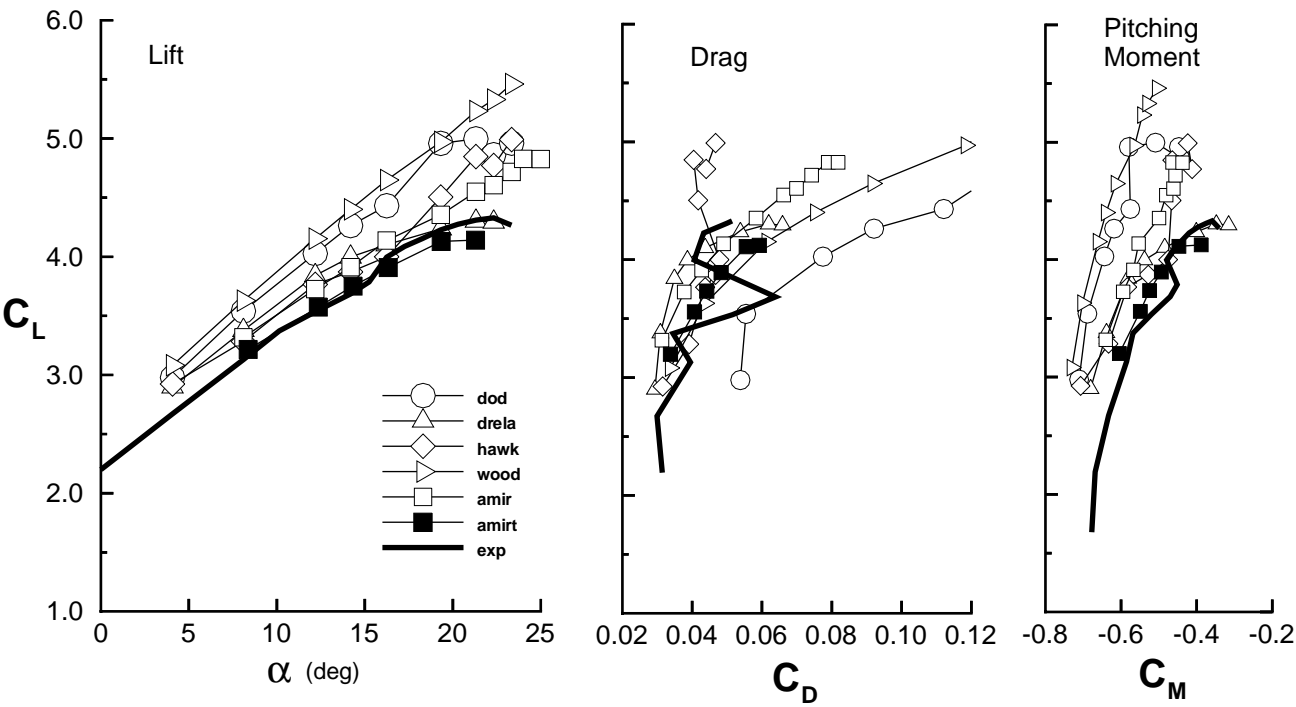
(a) Coupled Methods

(b) Reynolds Averaged Navier-Stokes Methods
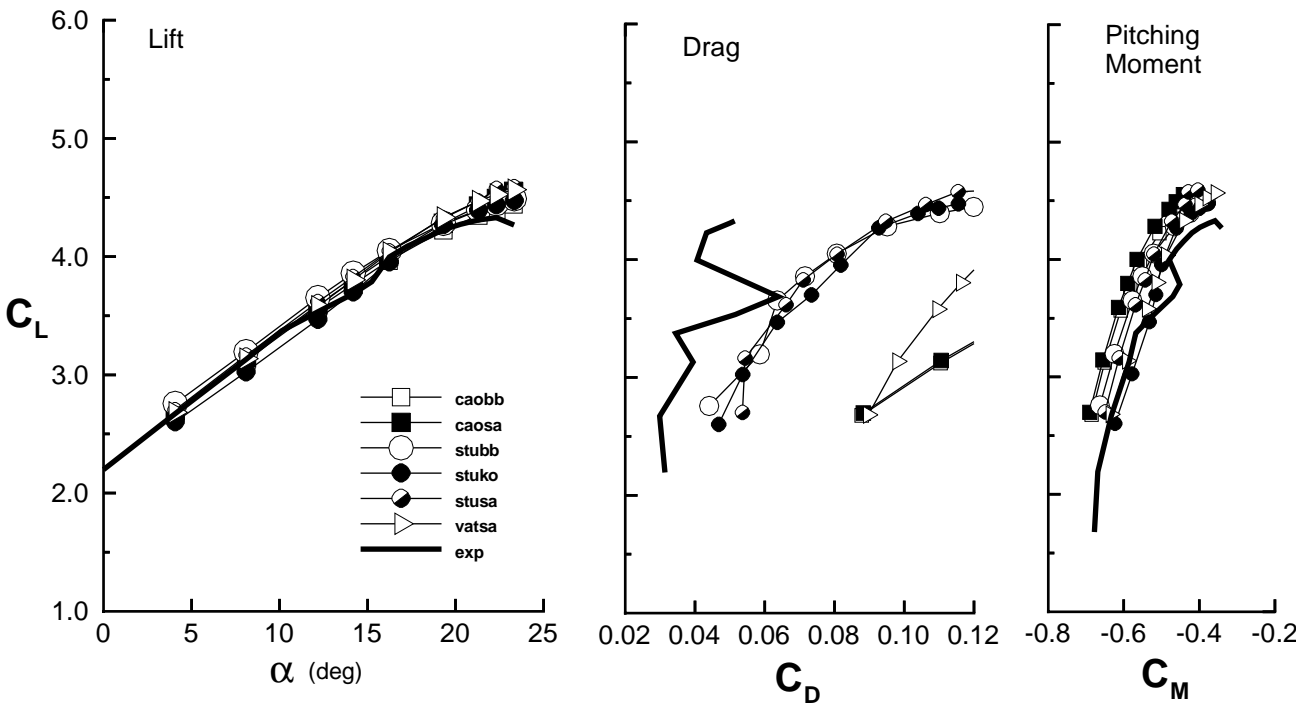
Figure 5. Force and moment coefficients for Geometry B, Re=9,000,000
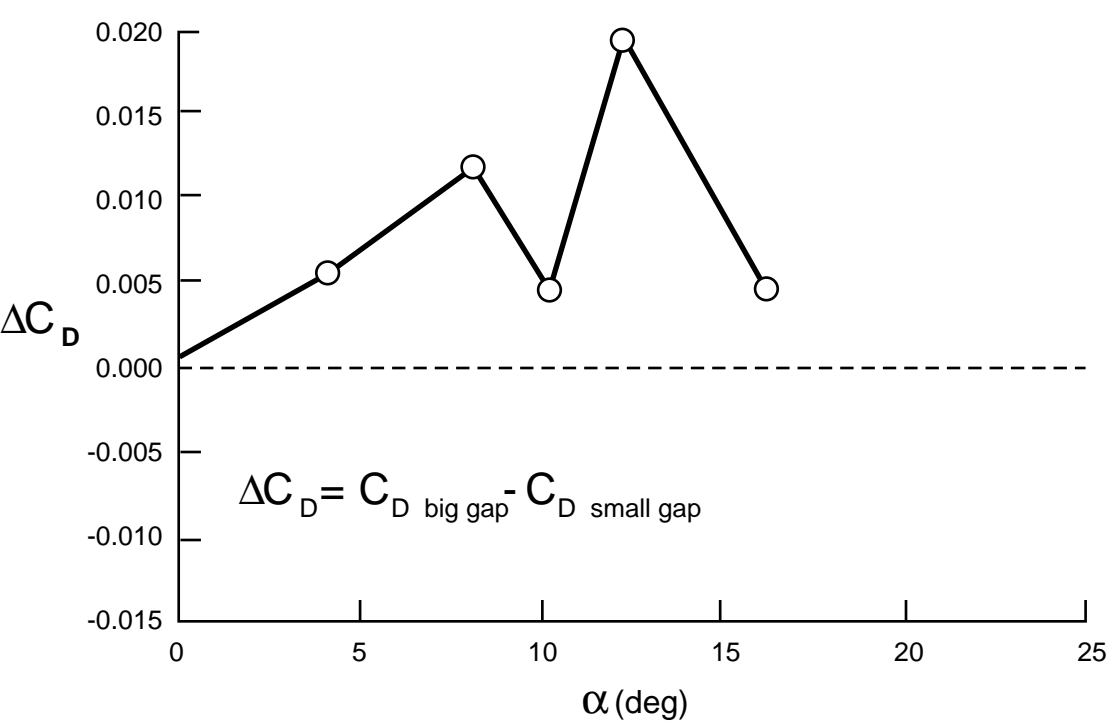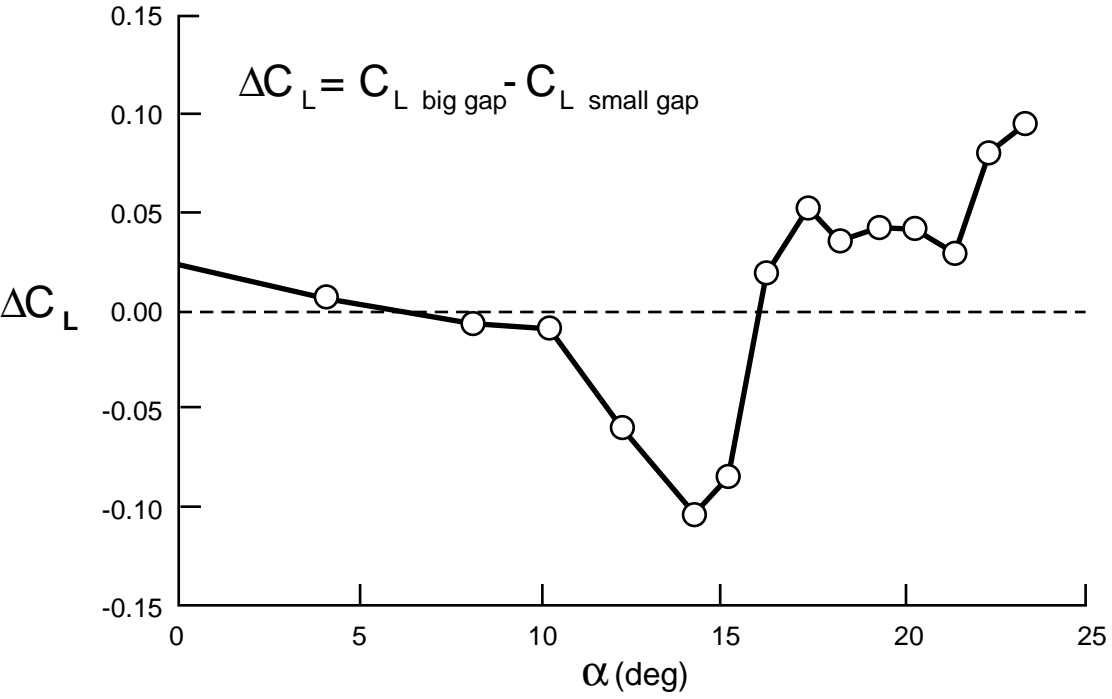
Figure 6. Lift and drag changes due to increase in flap gap, Re=9,000,000
        (Experiment -- LTPT)

Figure 7. Lift change due to increase in flap gap, Re=9,000,000
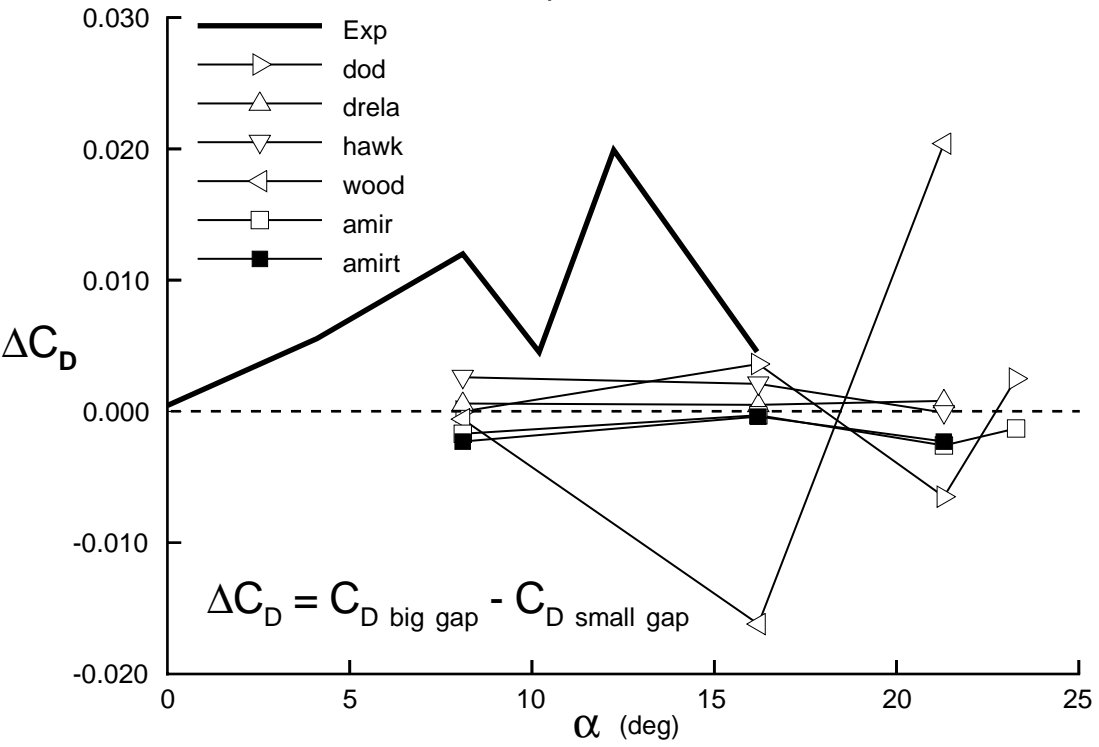
Figure 8. Drag change due to increase in flap gap, Re=9,000,000
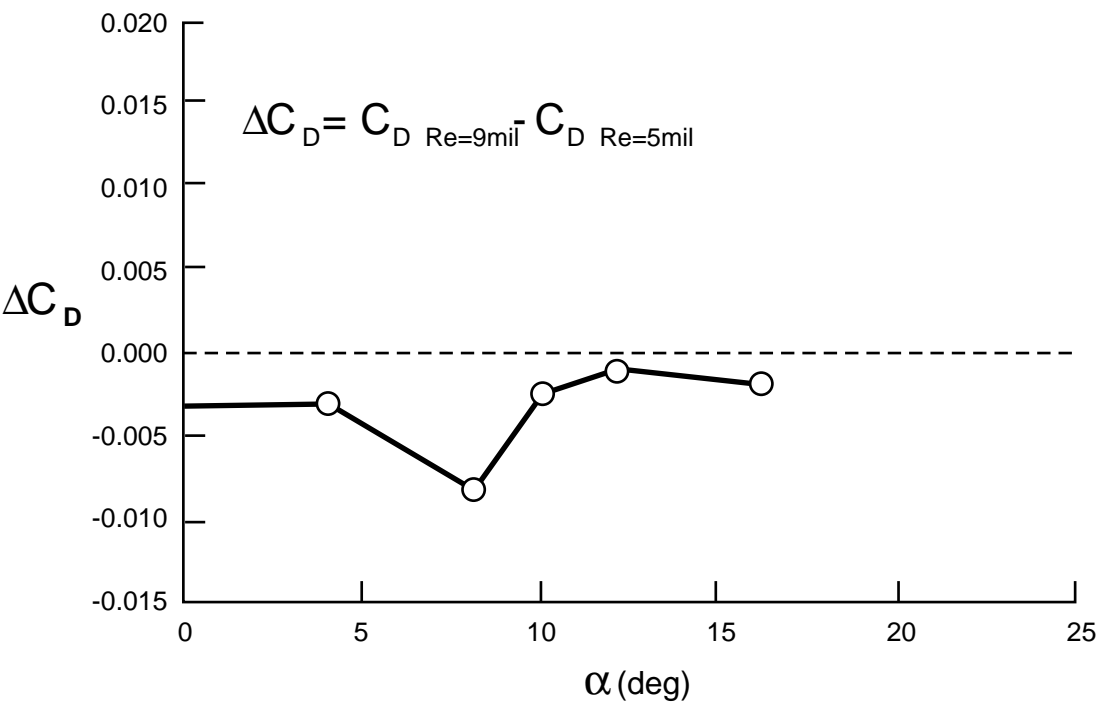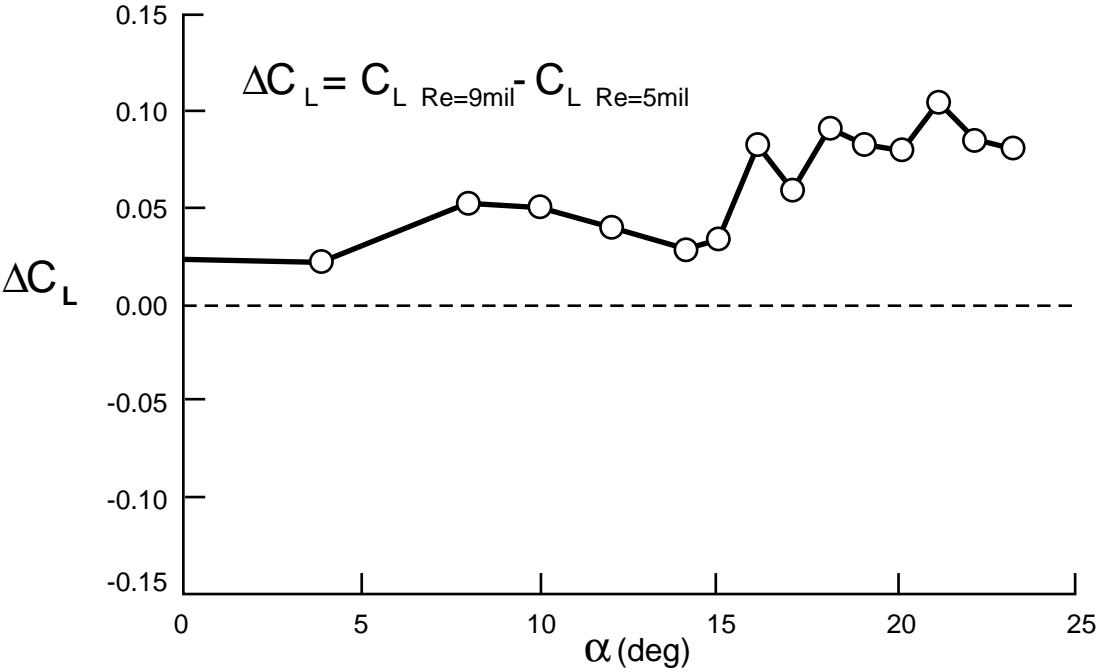
Figure 9. Lift and drag changes due to increase in Reynolds Number, Geometry A (Experiment -- LTPT)

Coupled Methods

$$\Delta C_L = C_{L\ Re=9\ mil} - C_{L\ Re=5\ mil}$$

Reynolds Averaged Navier-Stokes Methods

$$\Delta C_L = C_{L\ Re=9\ mil} - C_{L\ Re=5\ mil}$$
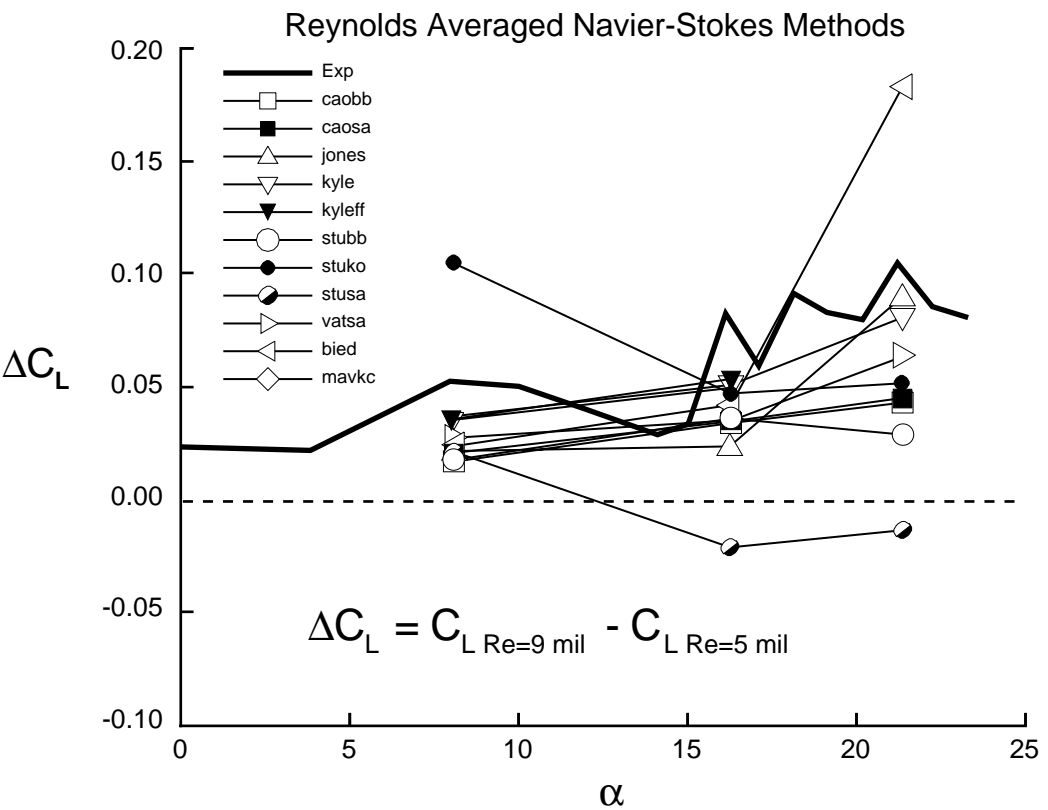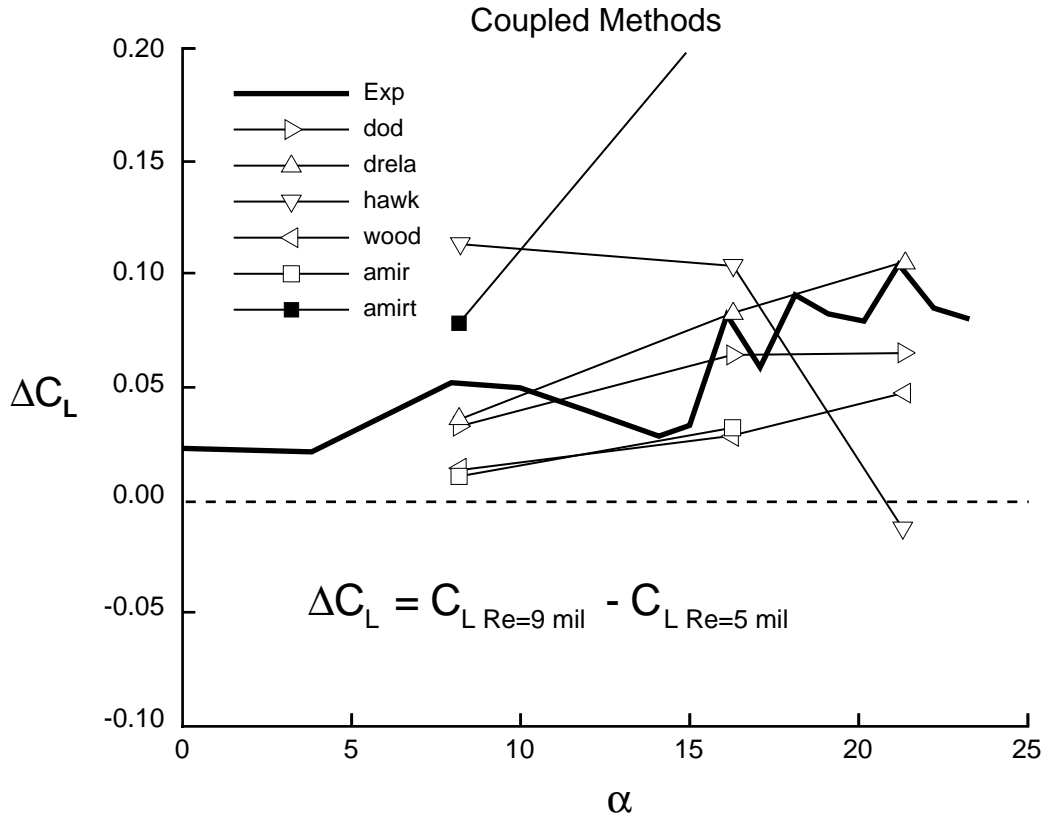
Figure 10. Lift change due to Reynolds Number increase, Geometry A

Coupled Methods

$$\Delta C_D = C_{D\ Re=9mil} - C_{D\ Re=5mil}$$

Exp
dod
drela
hawk
wood
amir
amirt

ΔC_D

α (deg)

Reynolds Averaged Navier-Stokes Methods

Exp
caobb
caosa
jones
kyle
kyleff
stubb
stuko
stusa
vatsa
bied
mavkc

ΔC_D

$$\Delta C_D = C_{D\ Re=9mil} - C_{D\ Re=5mil}$$

α (deg)
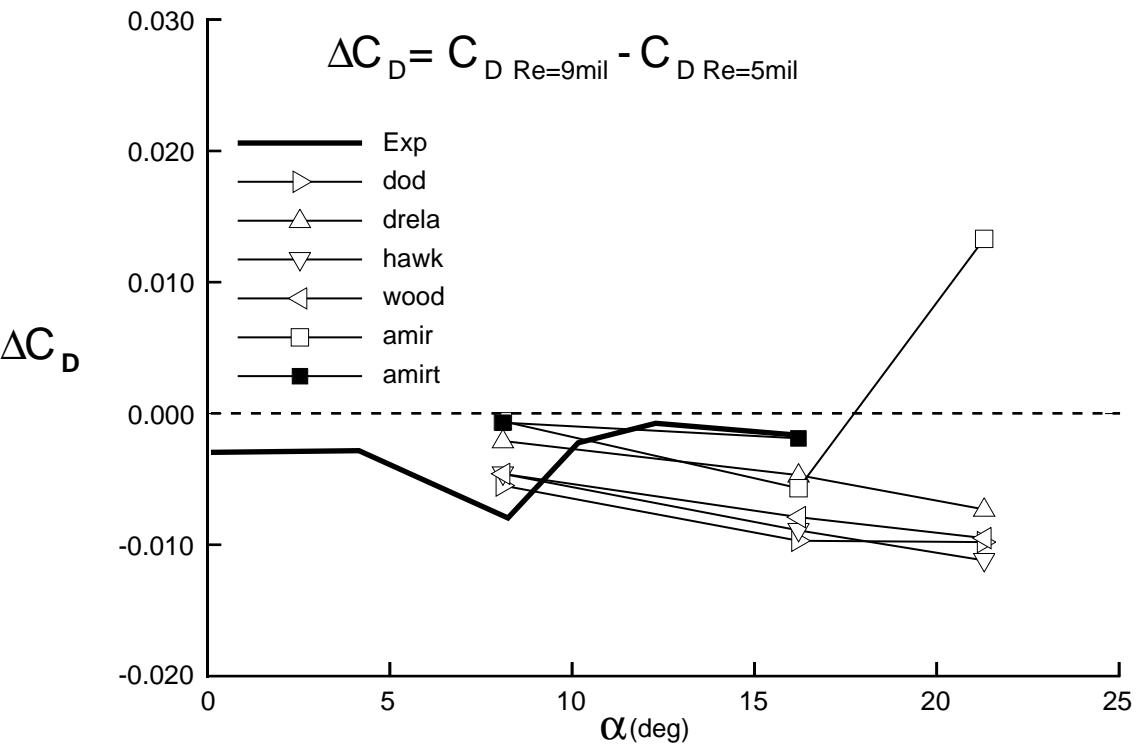
Figure 11. Drag change due to increase in Reynolds Number, Geometry A

29
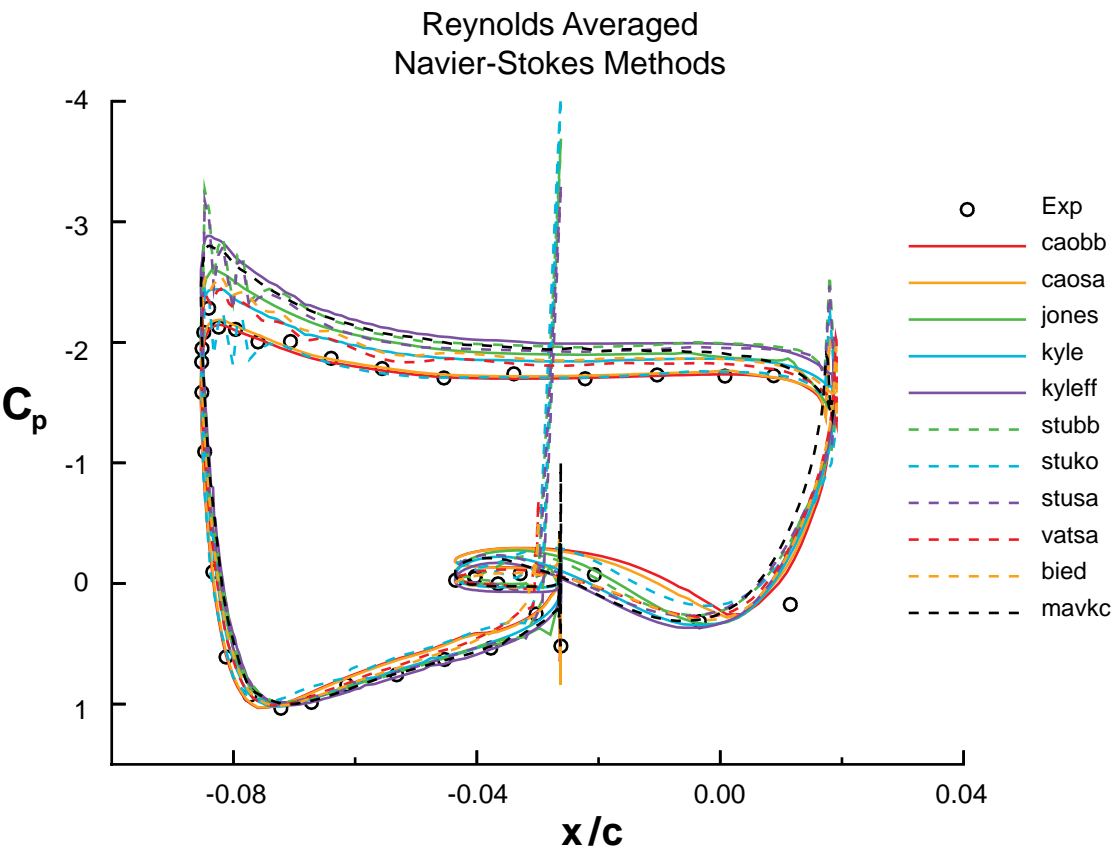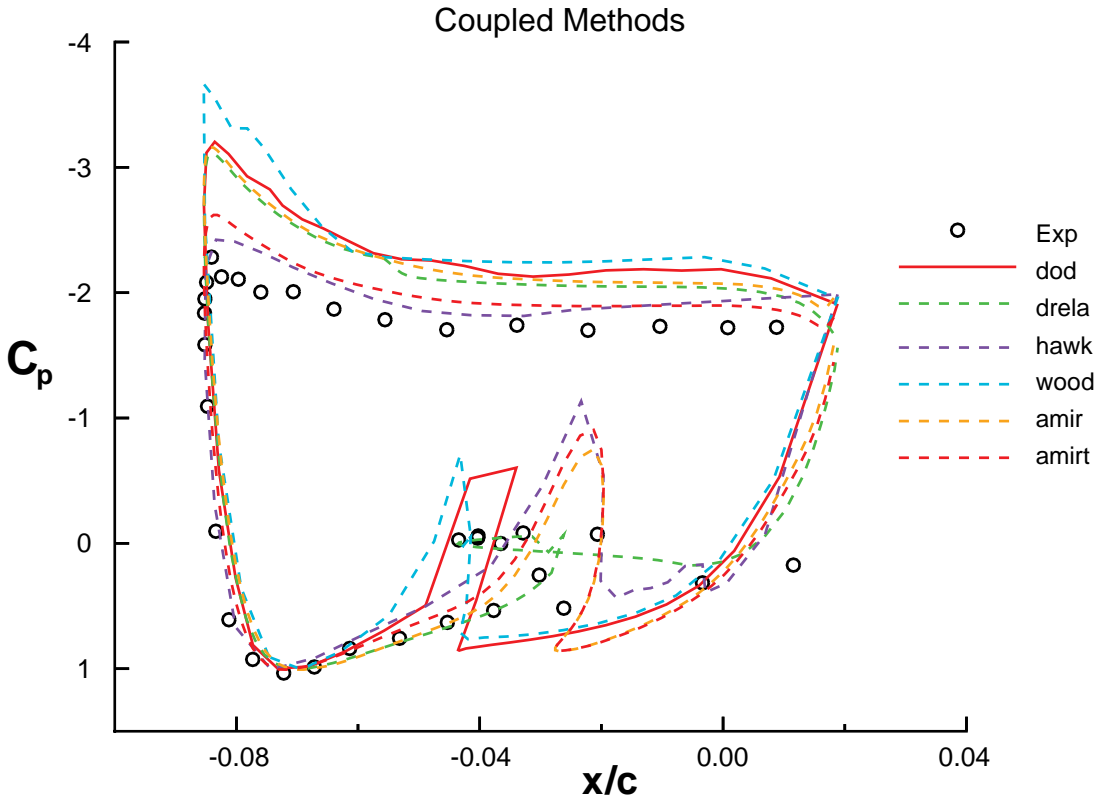
Figure 12. Slat pressure distribution -- Geometry A (α=8.12°, Re=5 million)

Figure 13. Main-element pressure distribution -- Geometry A
(α=8.12°, Re=5 million)
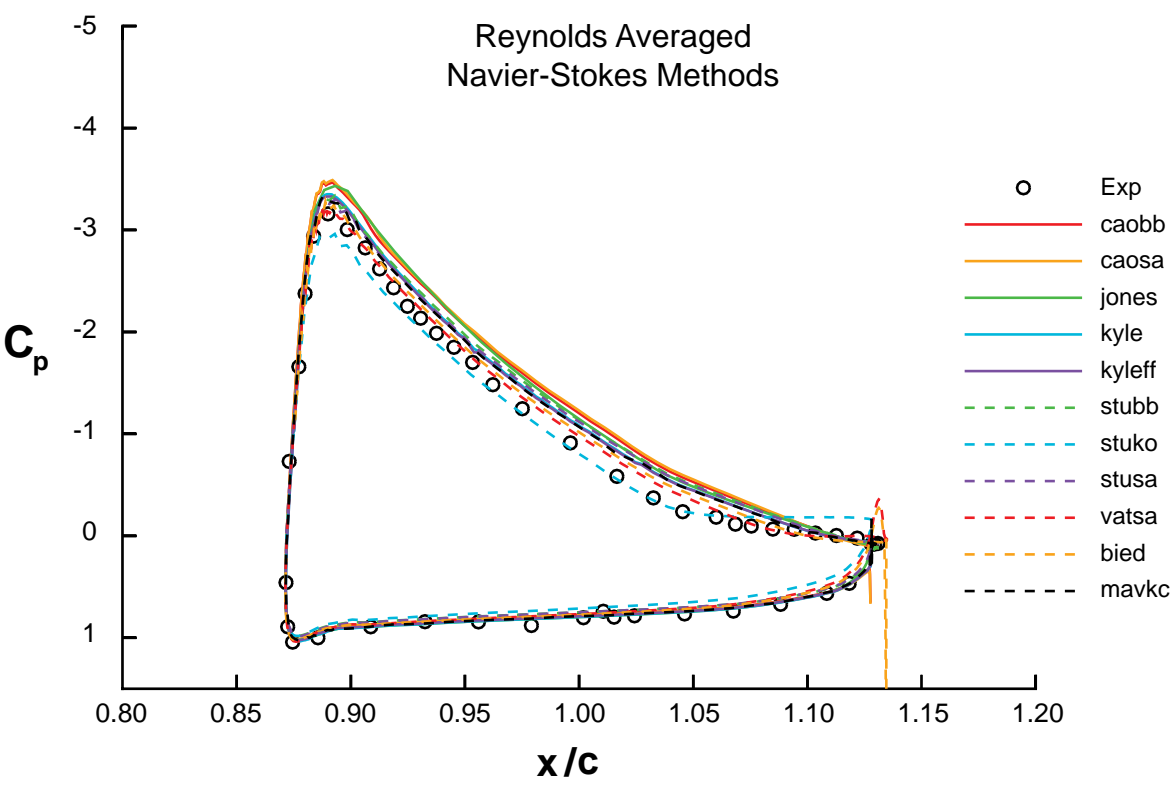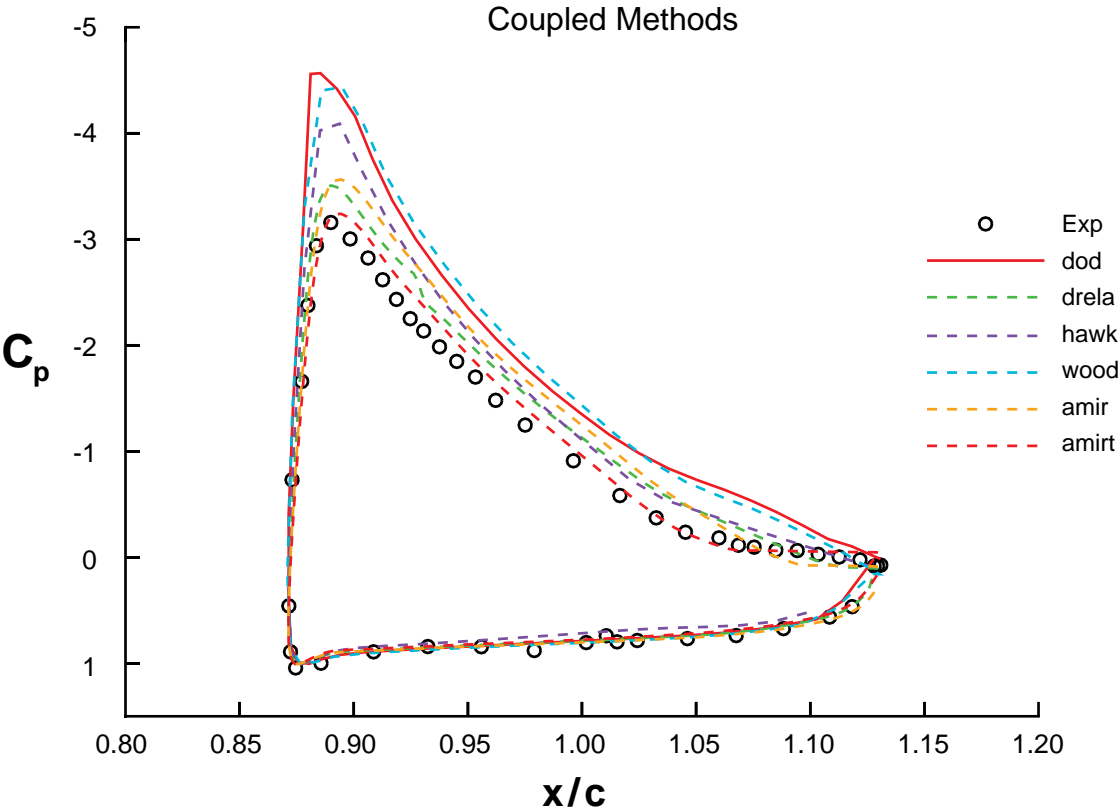
Figure 14. Flap pressure distribution -- Geometry A (α=8.12°, Re=5 million)
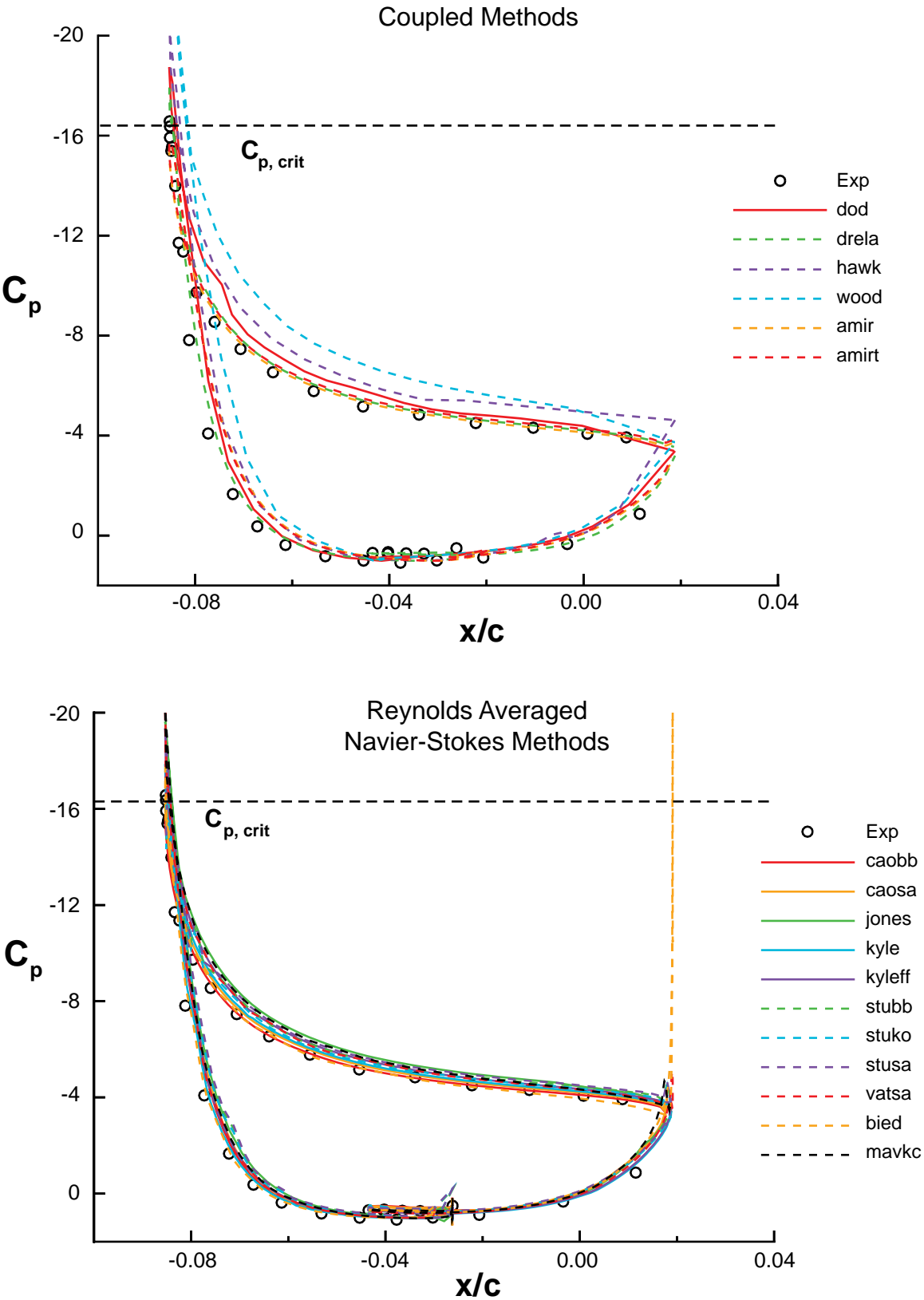
Figure 15. Slat pressure distribution -- Geometry A (α=21.29°, Re=5 million)
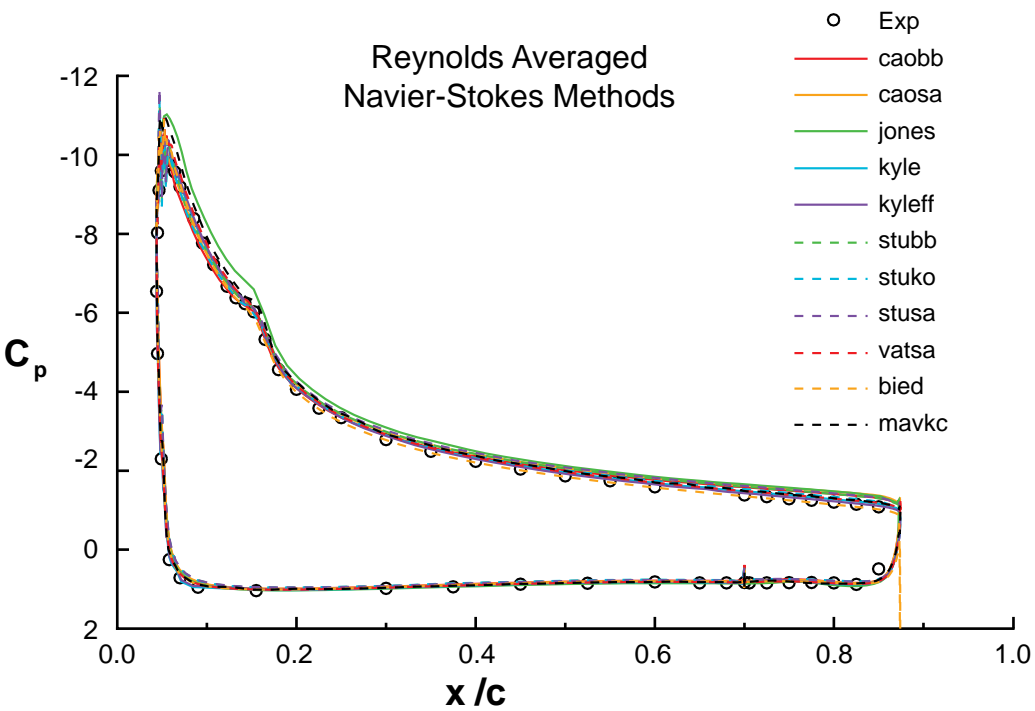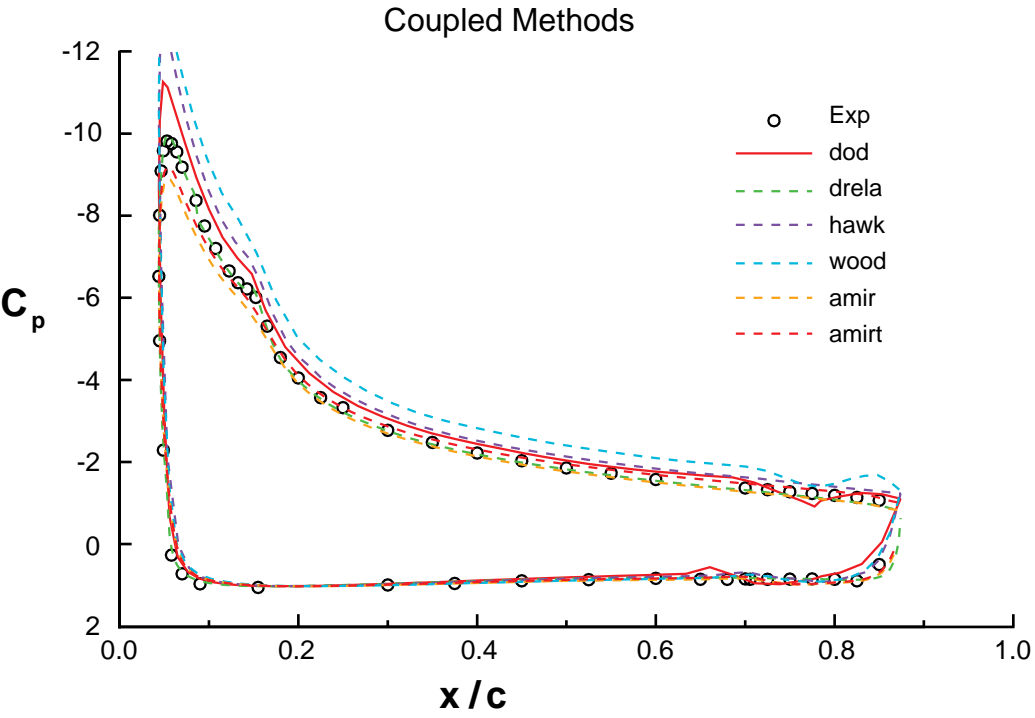
Figure 16. Main-element pressure distribution -- Geometry A
(α = 21.29°, Re = 5 million)

34
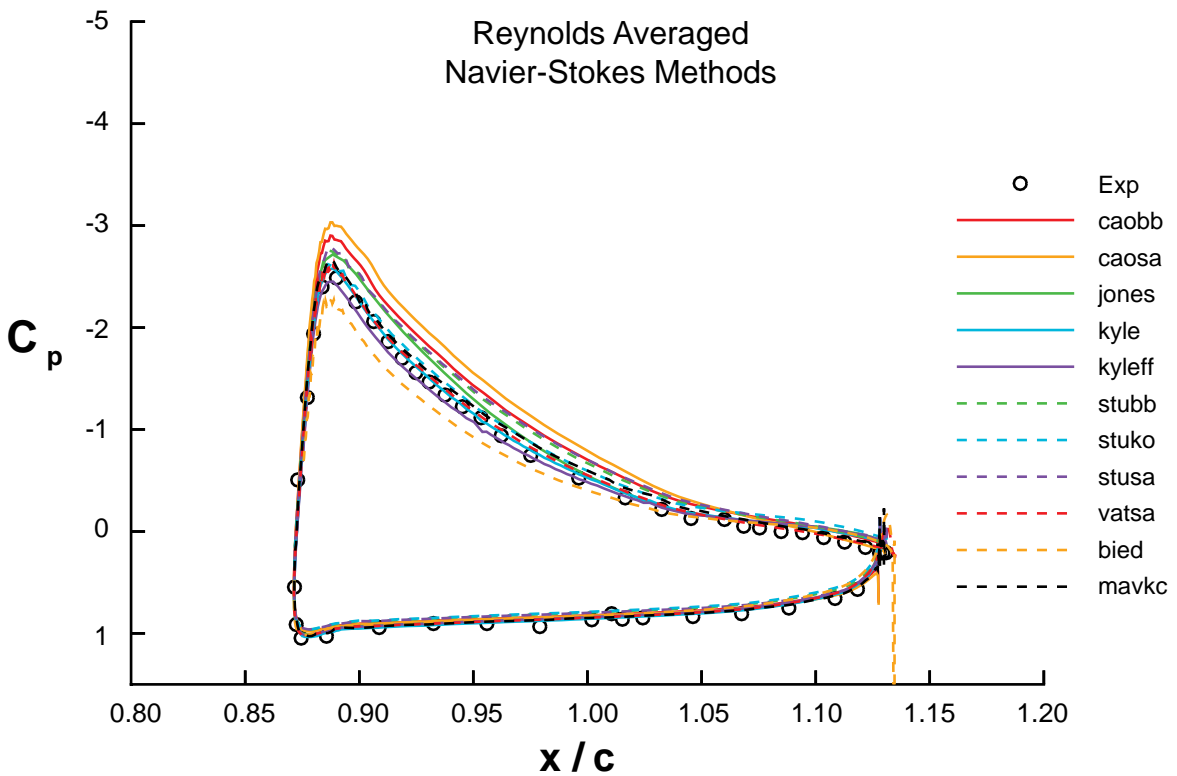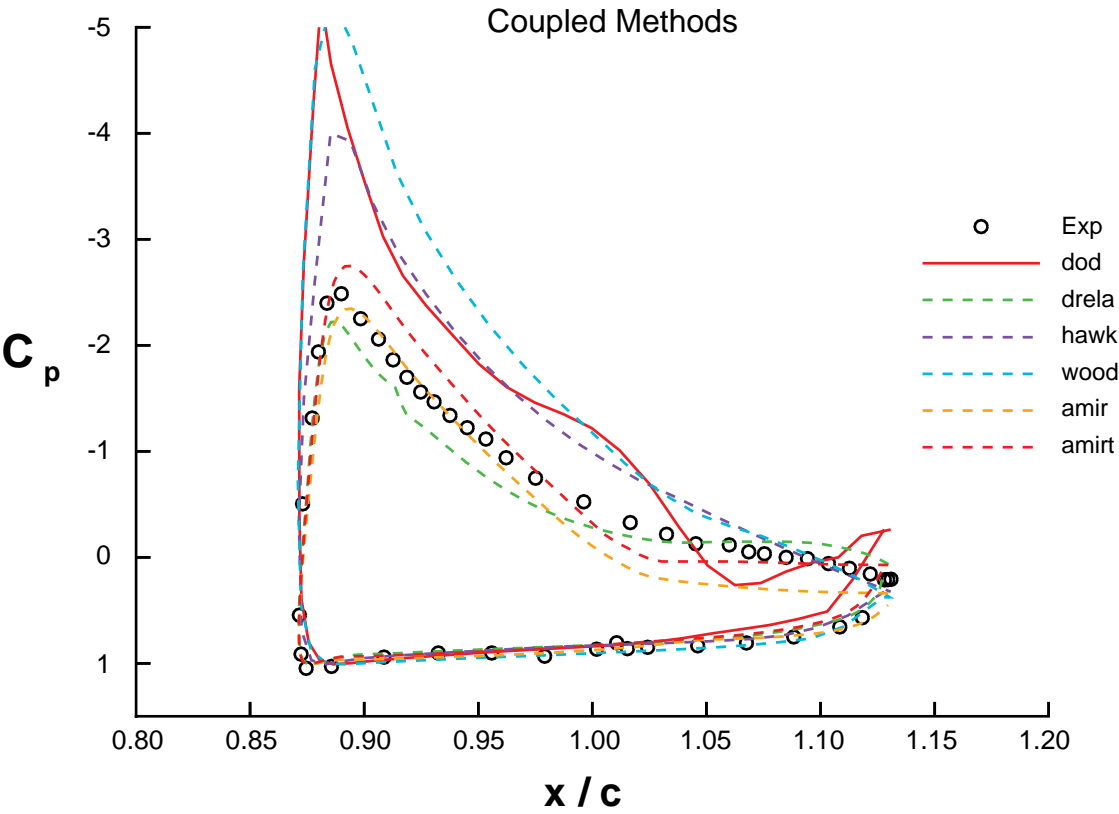
Figure 17. Flap pressure distribution -- Geometry A (α=21.29°, Re=5 million)
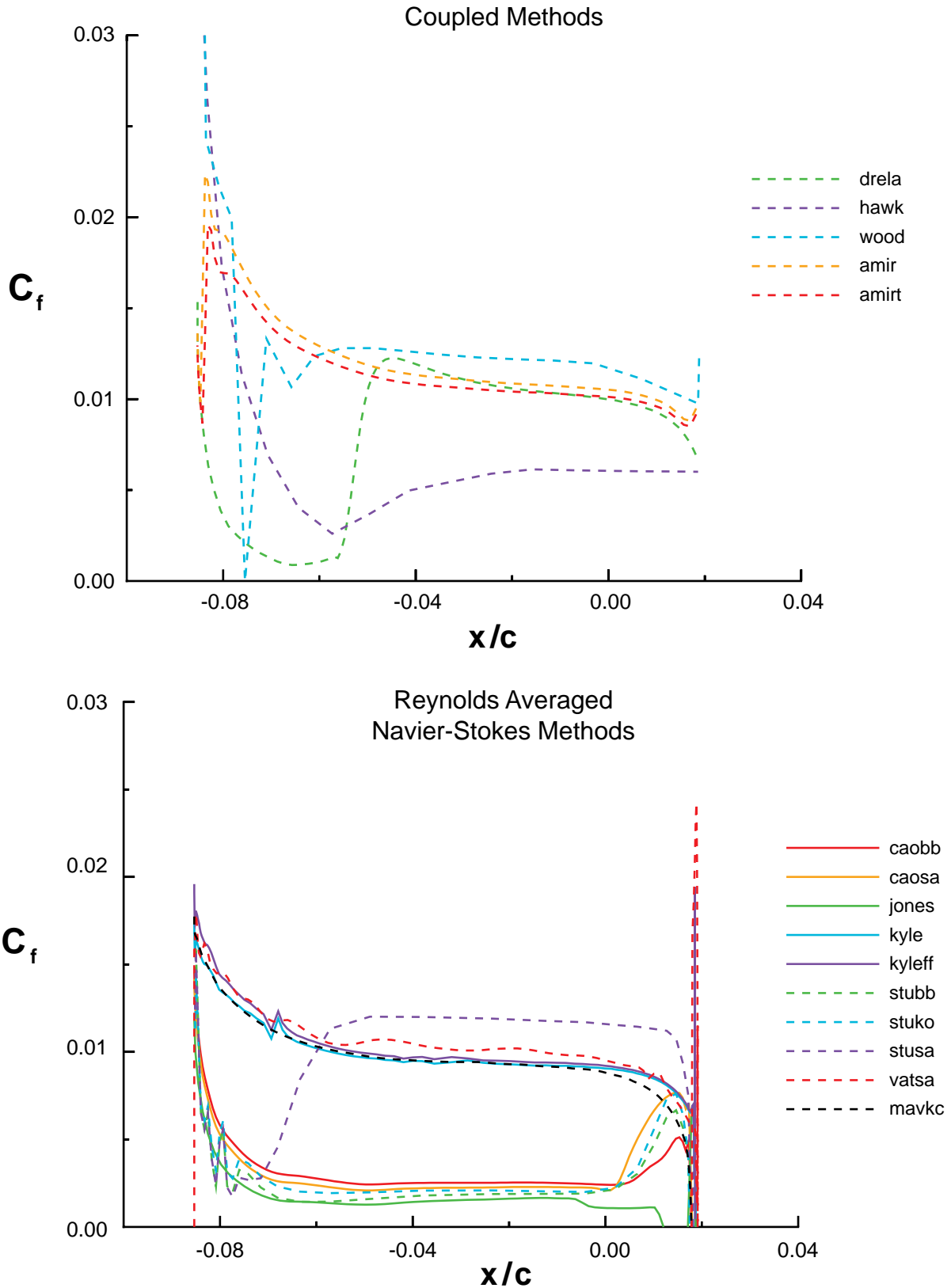
Figure 18. Slat skin-friction distribution -- Geometry A, upper surface only
(α=8.12°, Re=5 million)

Coupled Methods
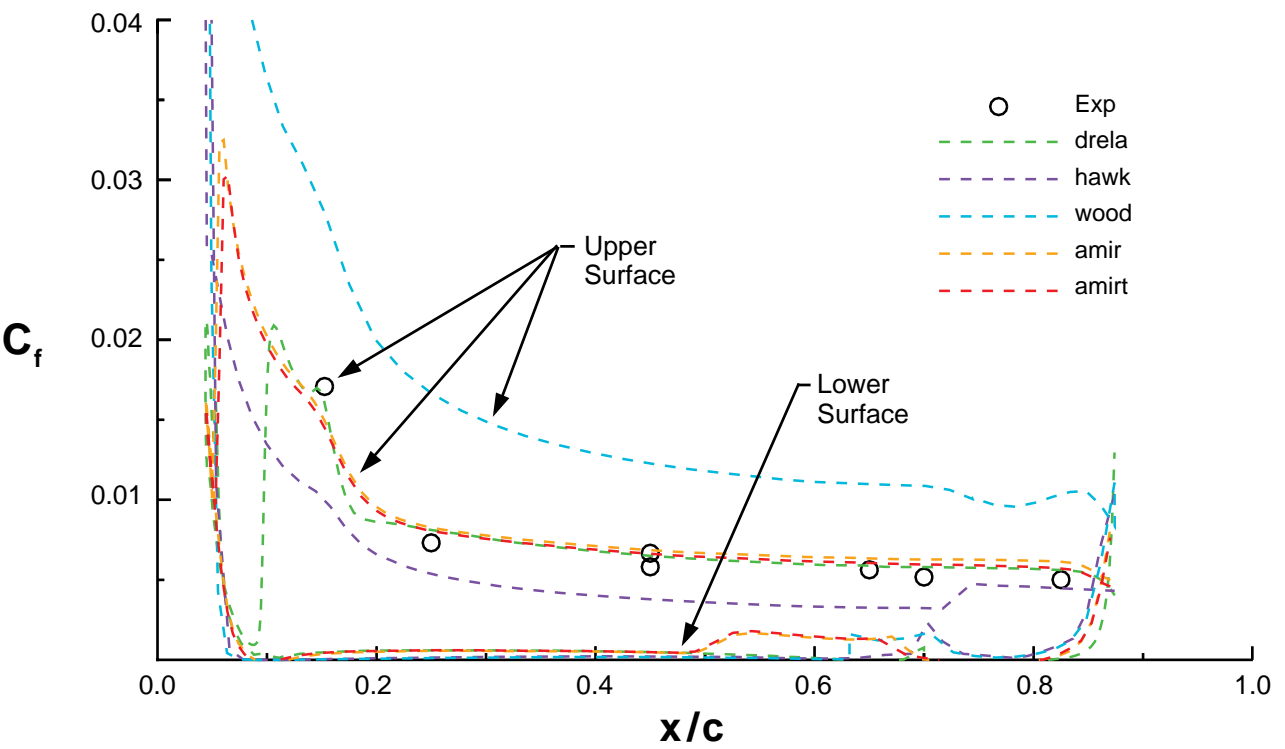
Reynolds Averaged
Navier-Stokes Methods
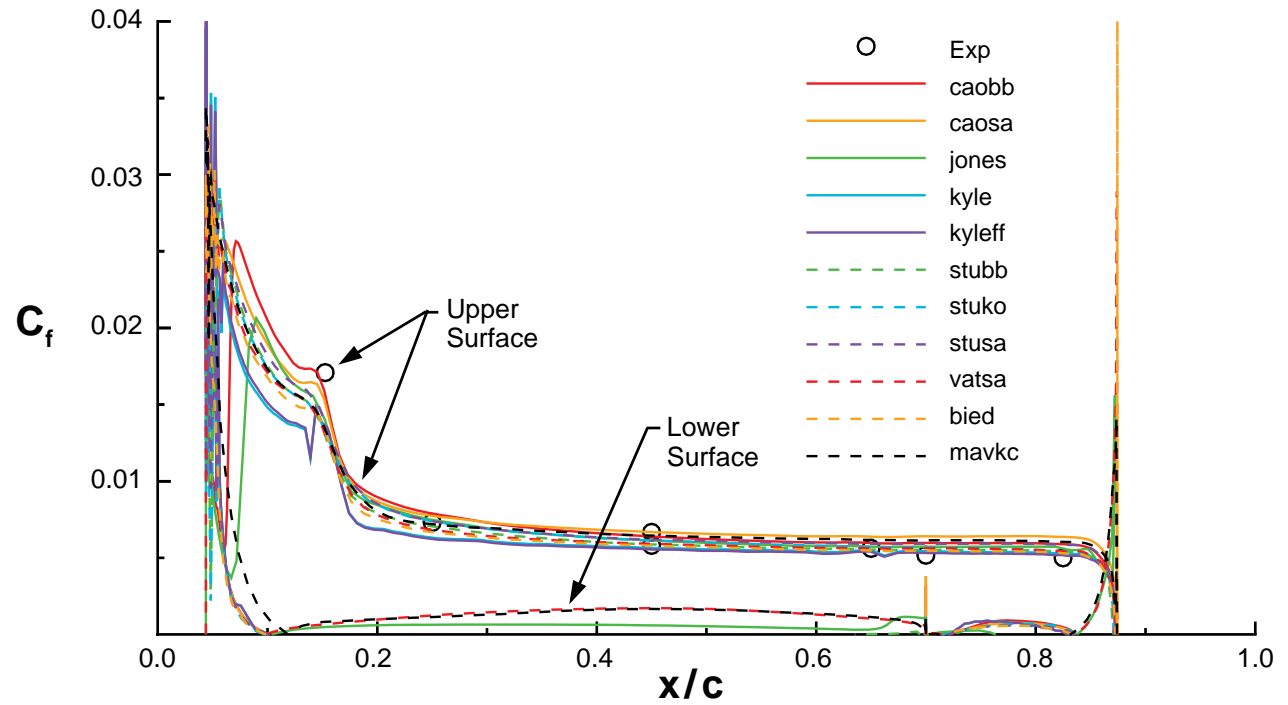
Figure 19. Main-element skin-friction distribution -- Geometry A
(α=8.12$\degree$, Re=5 million)
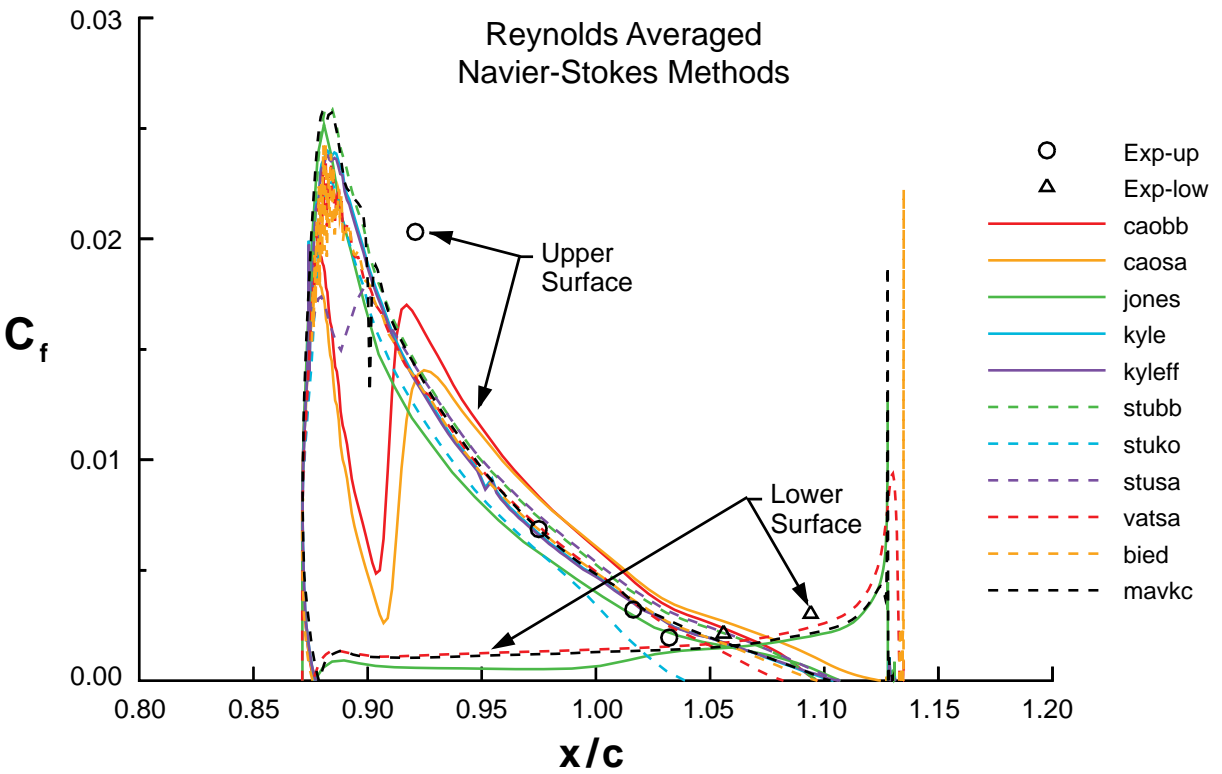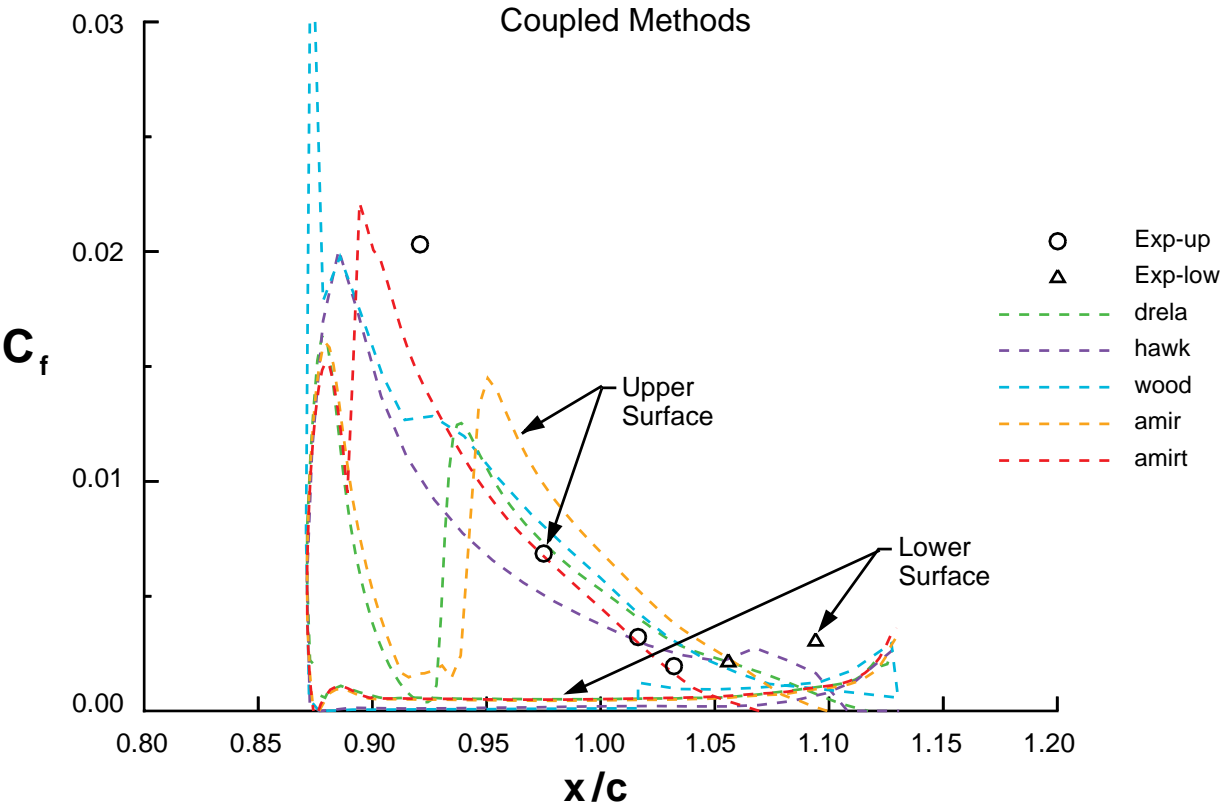
Figure 20. Flap skin-friction distribution -- Geometry A (α=8.12°, Re=5 million)
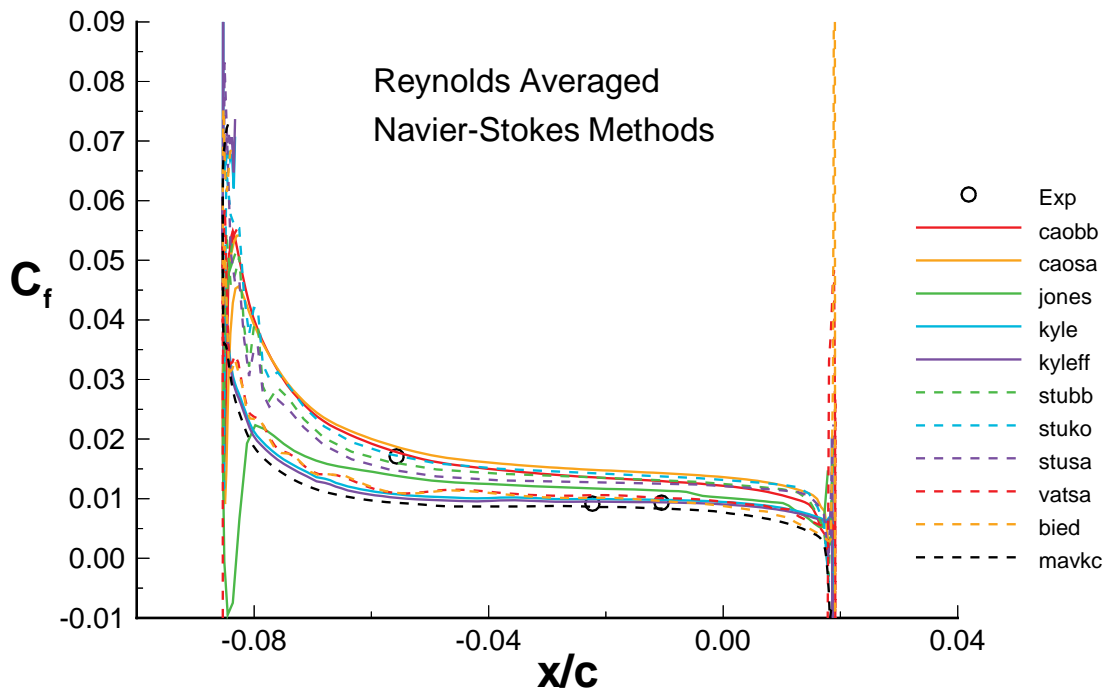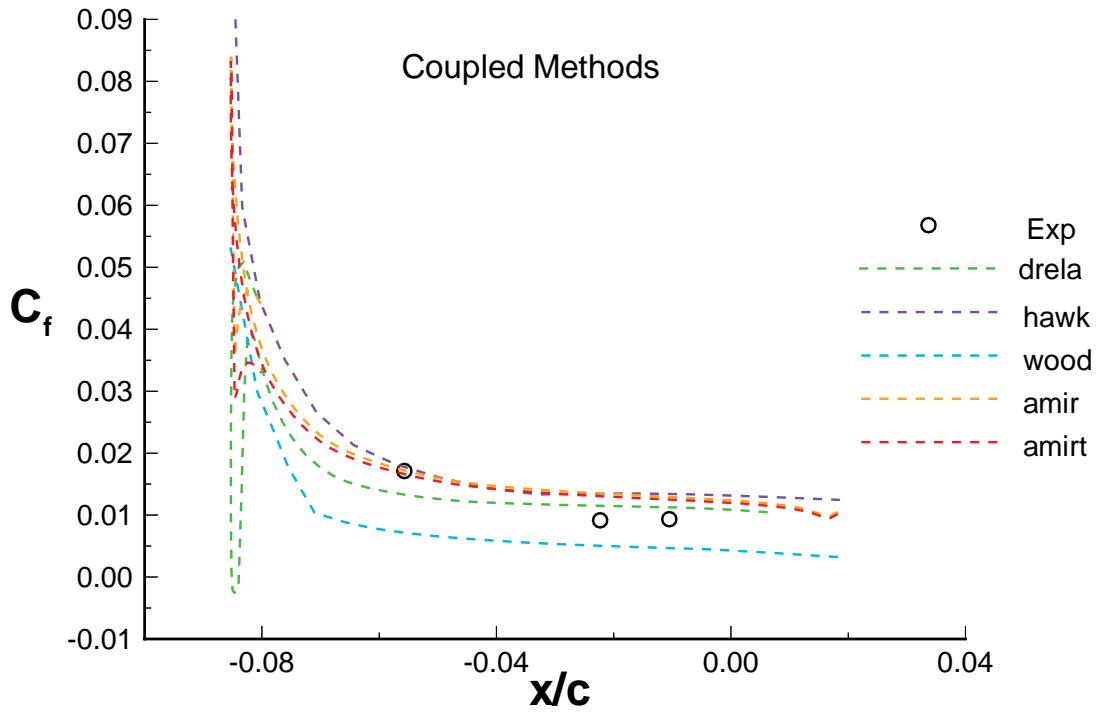
Figure 21. Slat skin-friction distribution -- Geometry A, upper surface only
(α=21.29°, Re=5 million)
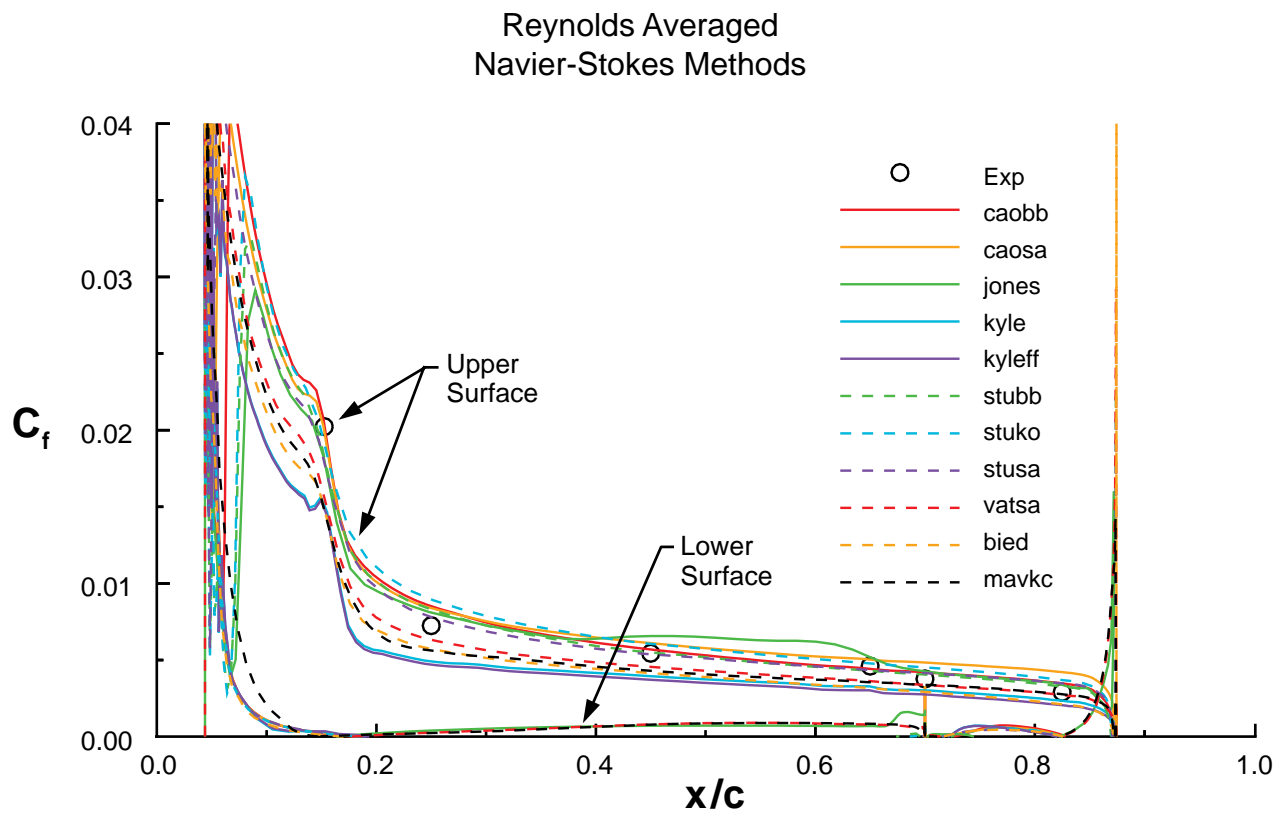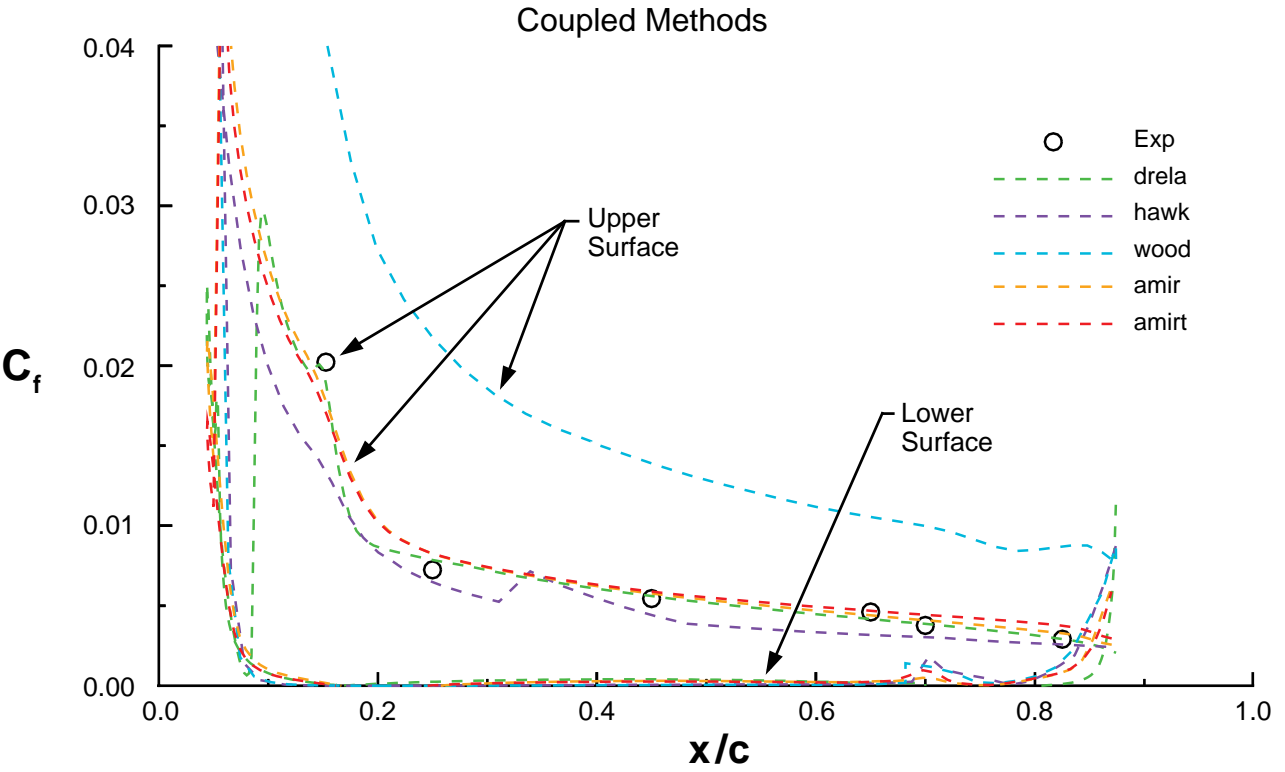
Figure 22. Main-element skin-friction distribution -- Geometry A (α=21.29°, Re=5 million)
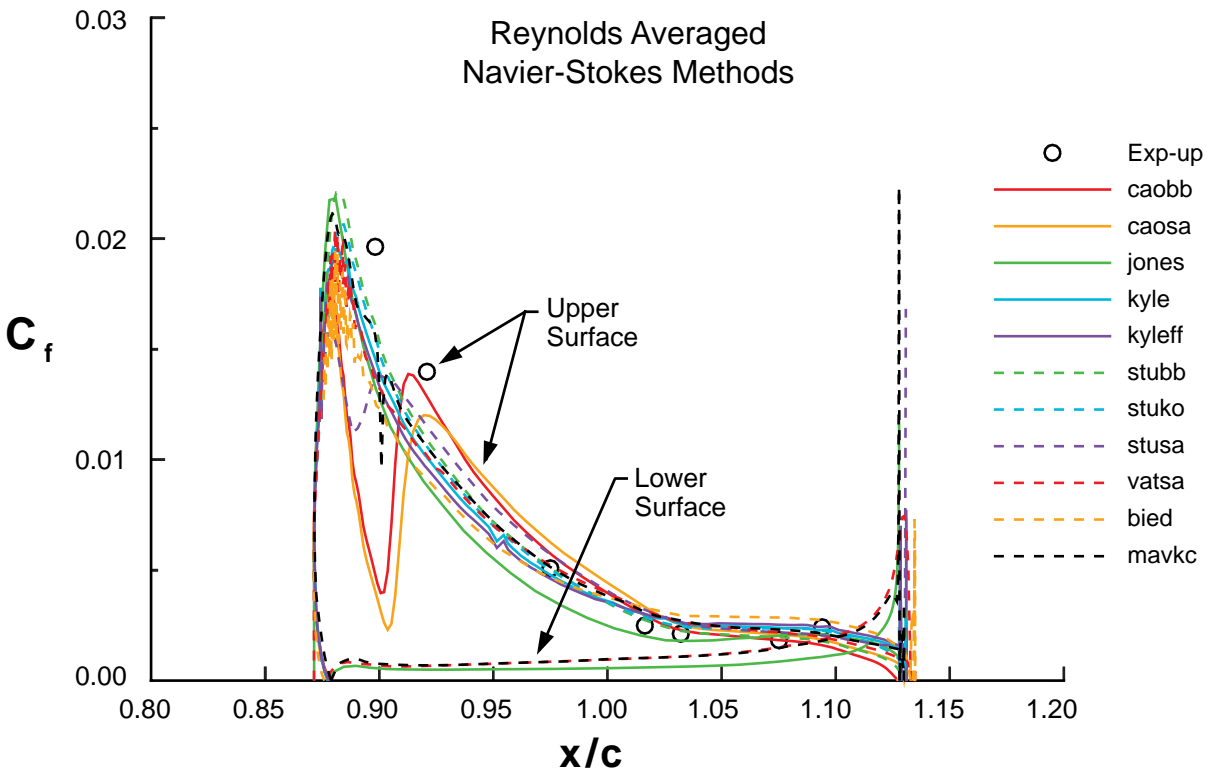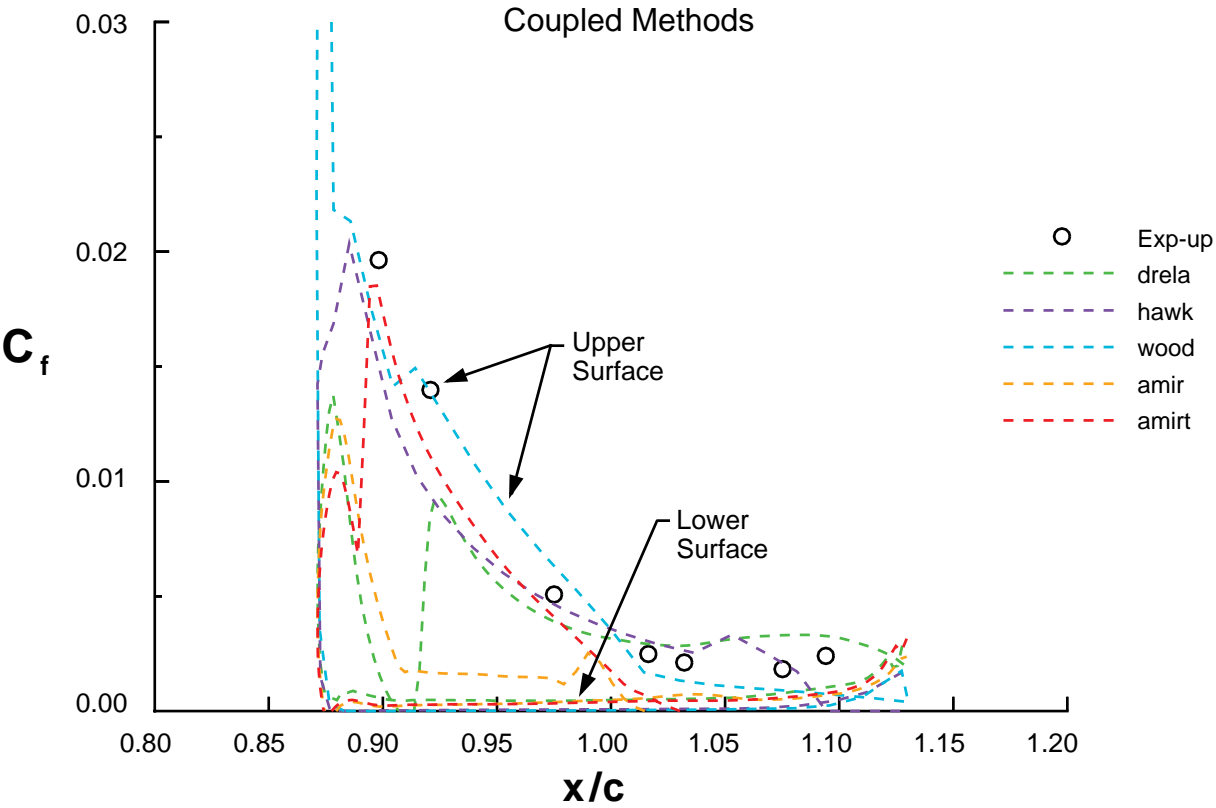
Figure 23. Flap skin-friction distribution -- Geometry A (α=21.29°, Re=5 million)
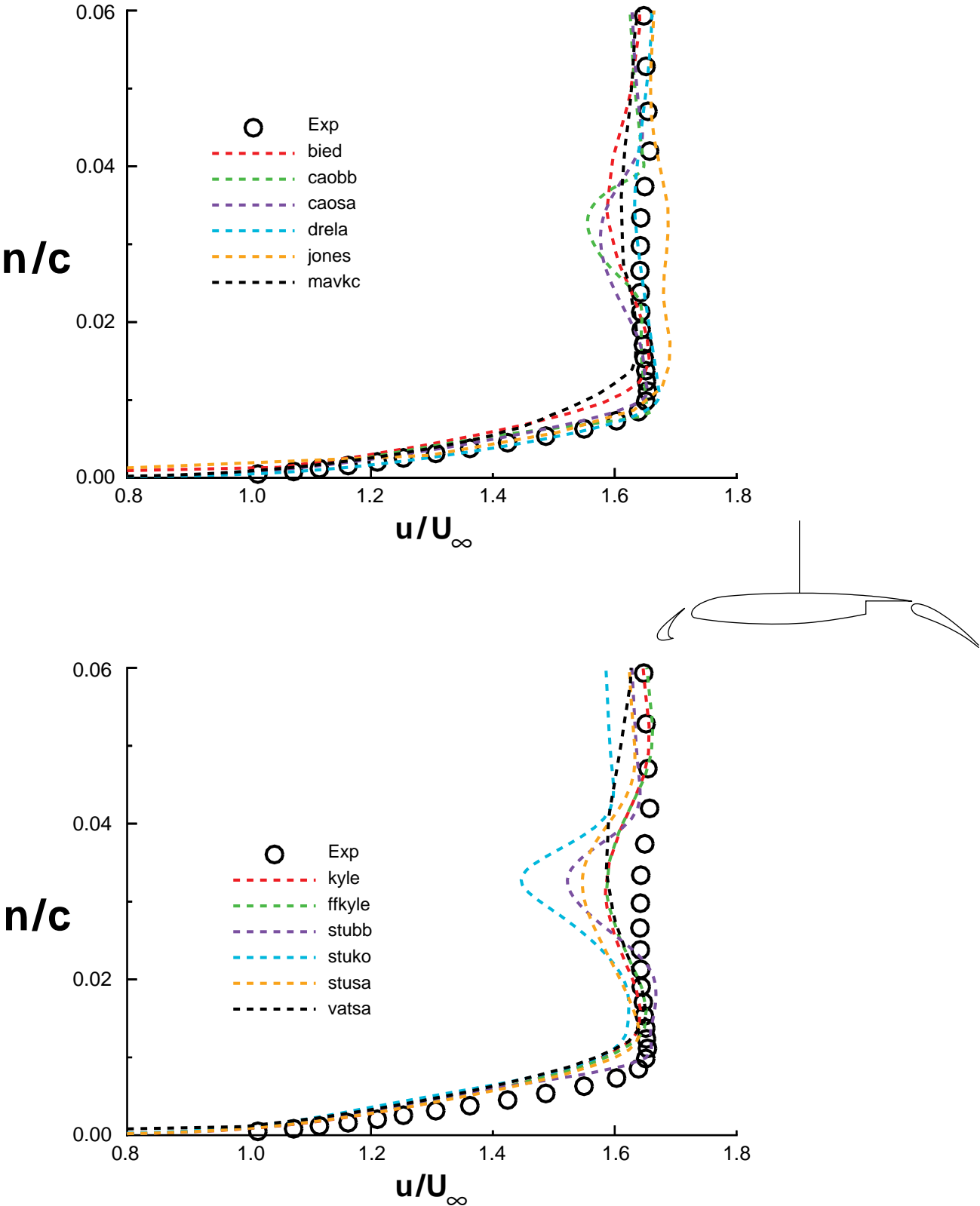
Figure 24. Velocity profiles on the main element -- Geometry A
(x/c=.45, α=8.12°, Re=5 million)
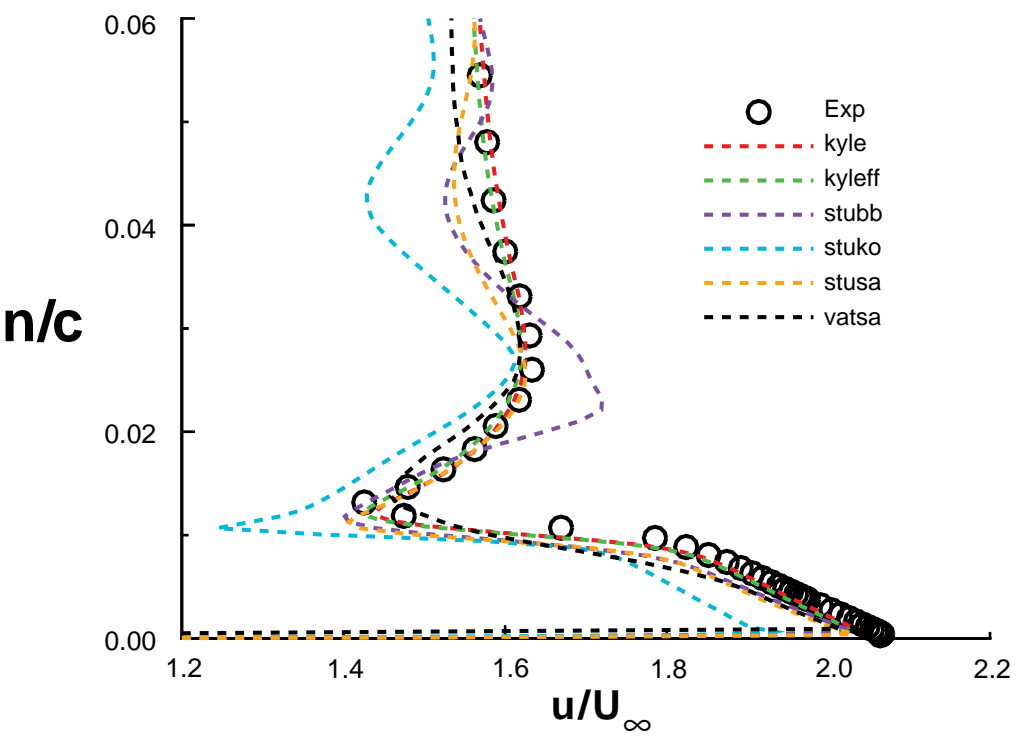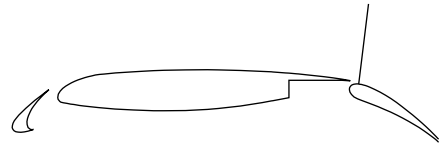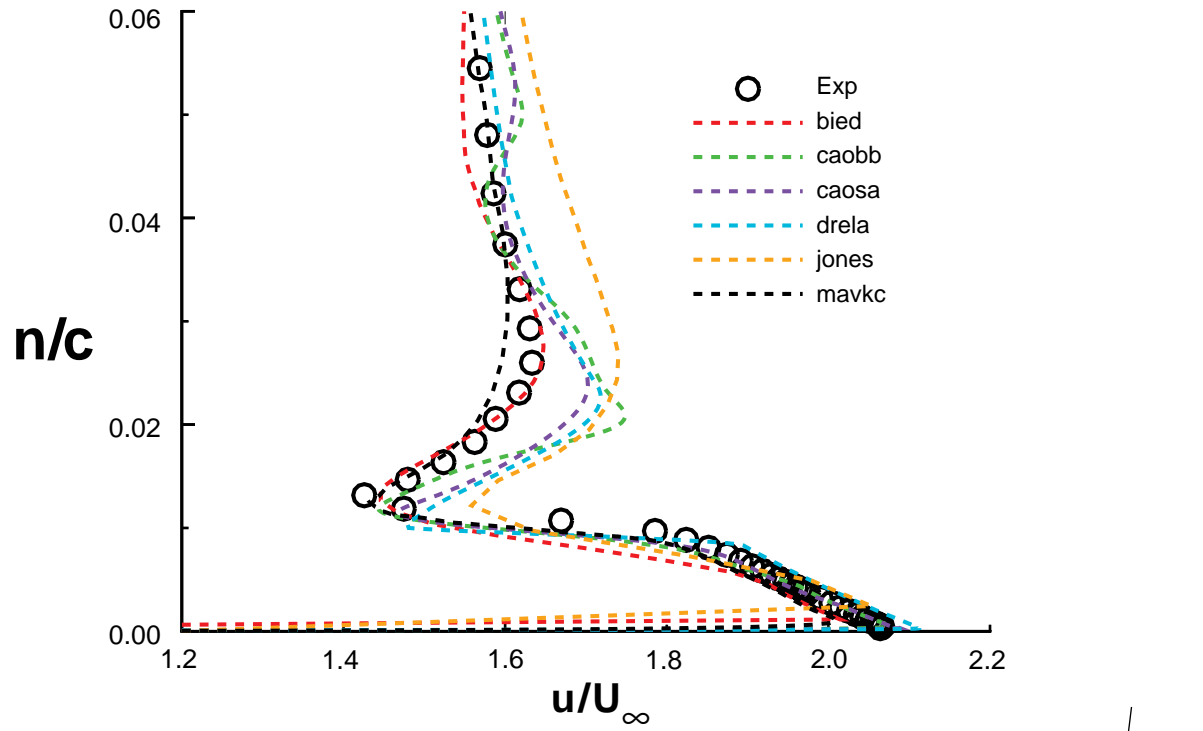
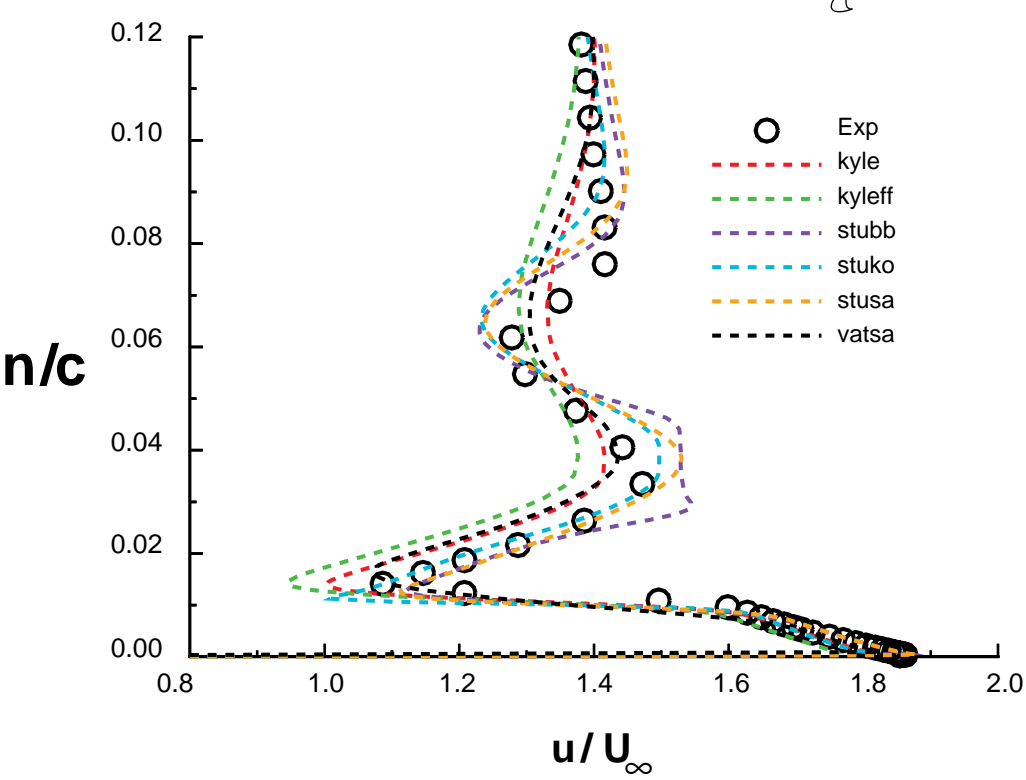Figure 25. Velocity profiles on the flap -- Geometry A
(x/c=.898, α=8.12°, Re=5 million)
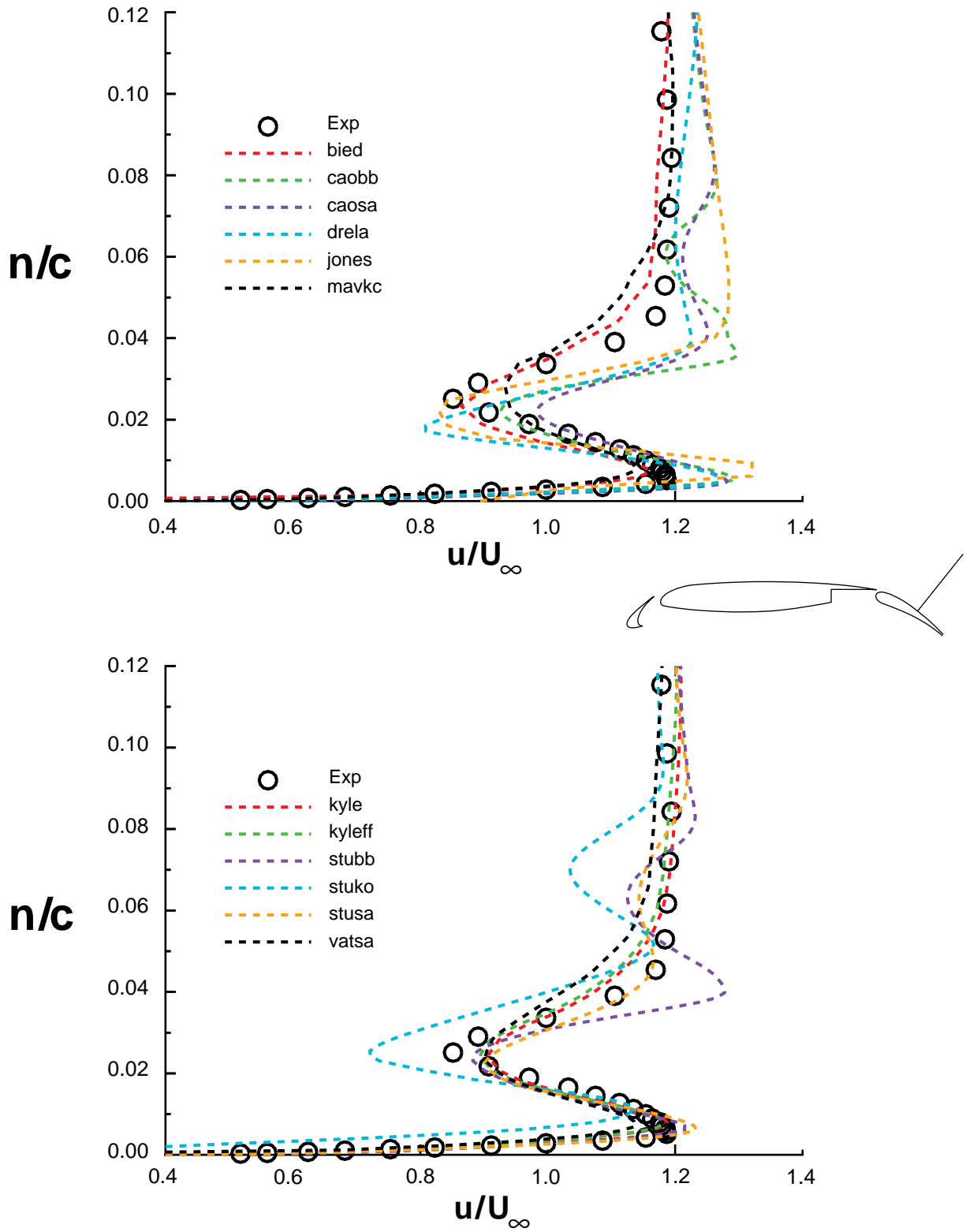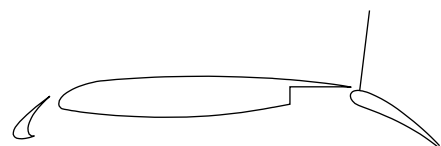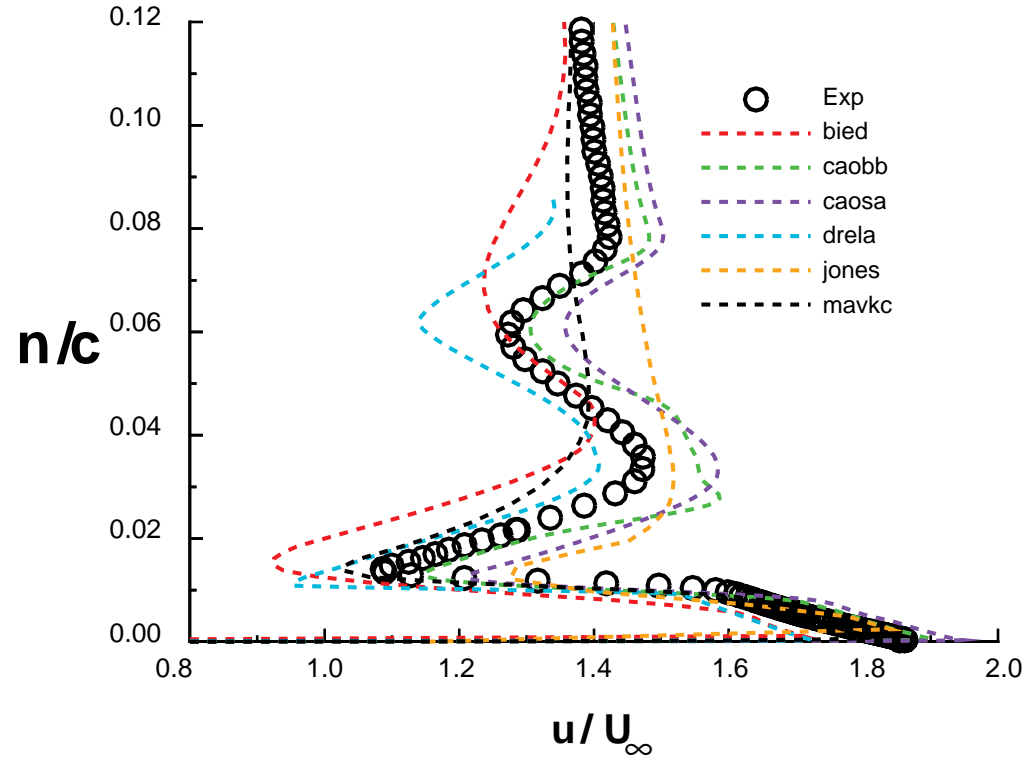
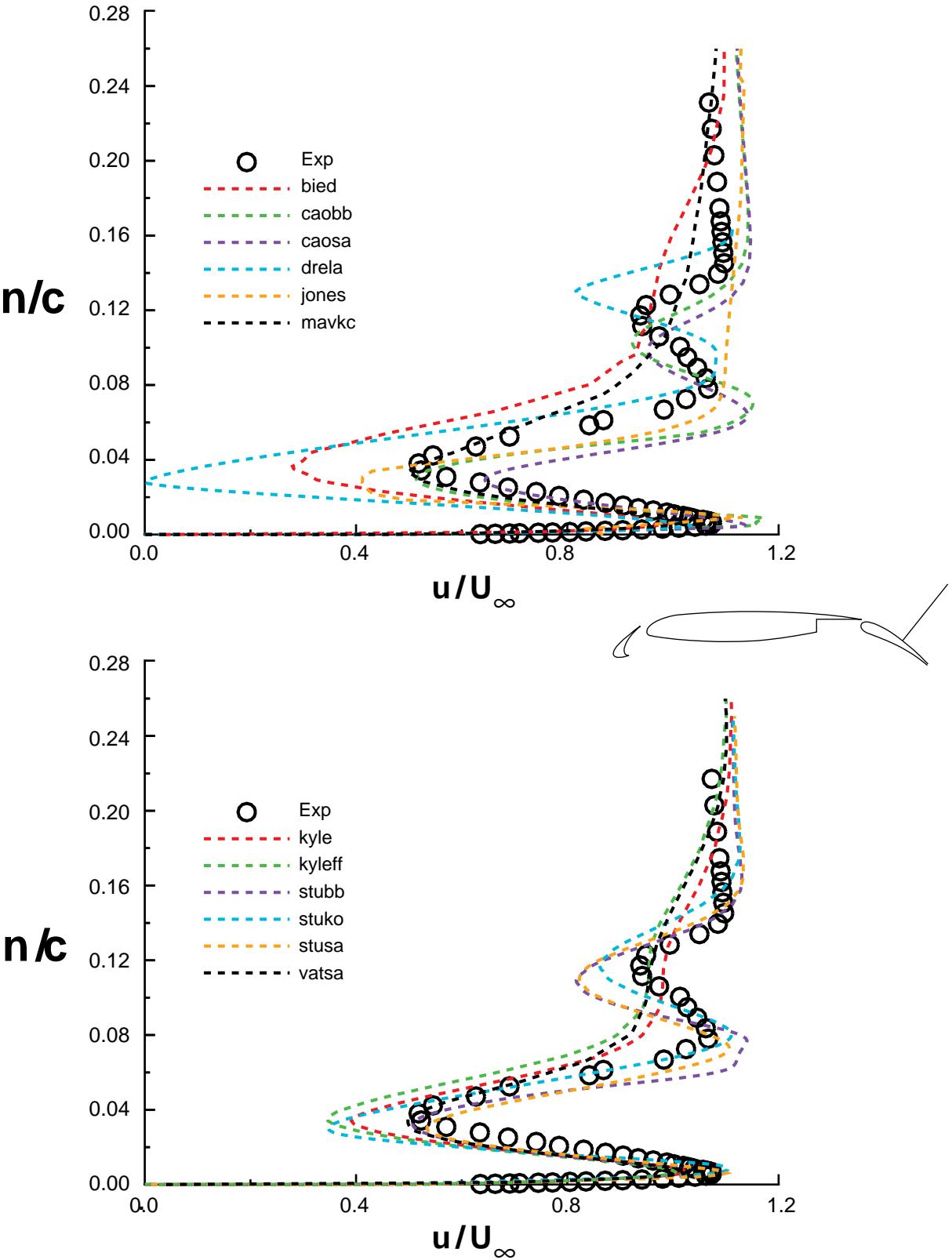Figure 26. Velocity profiles on the flap -- Geometry A
(x/c=1.032, α=8.12°, Re=5 million)
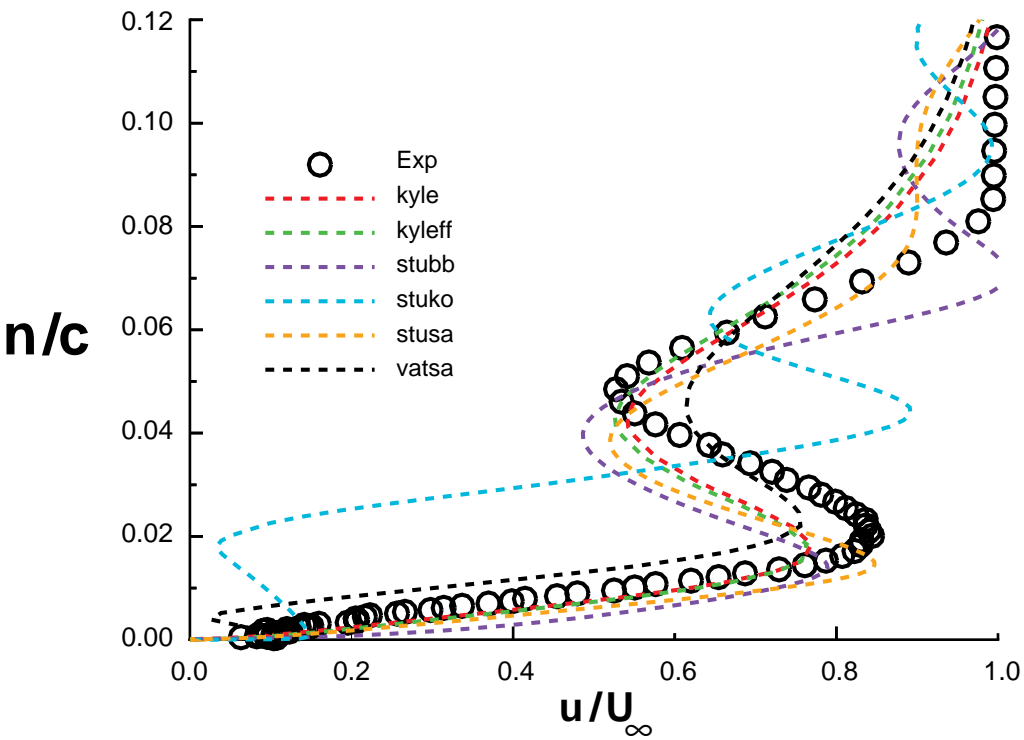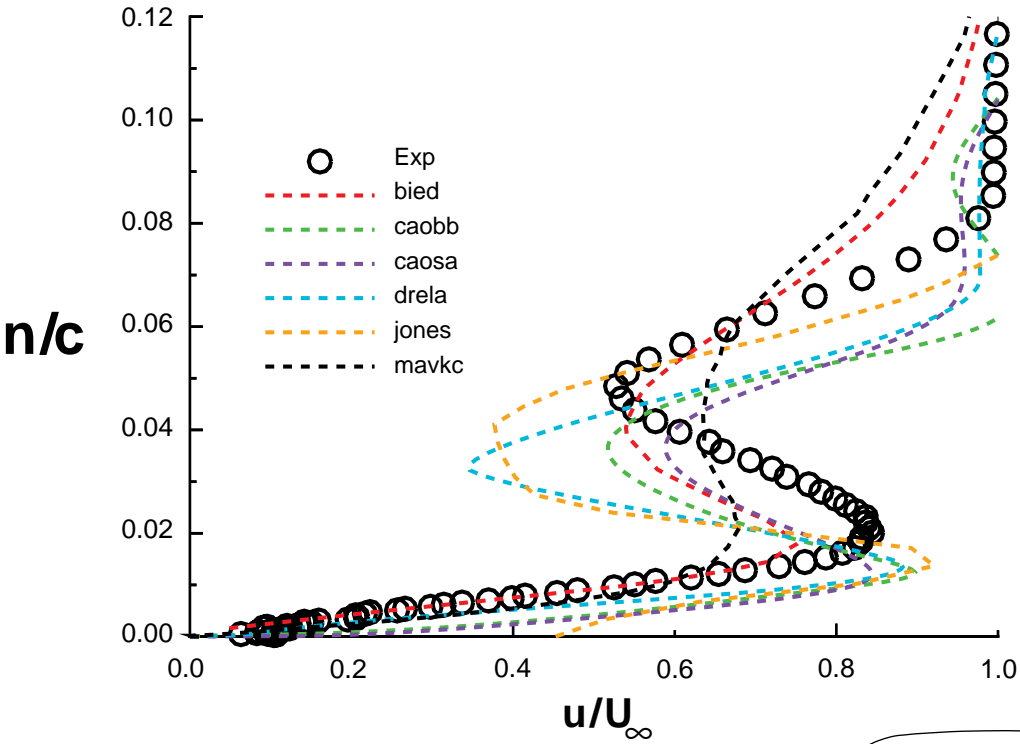
Figure 27. Velocity profiles on the flap -- Geometry A
(x/c=1.112, α=8.12°, Re=5 million)
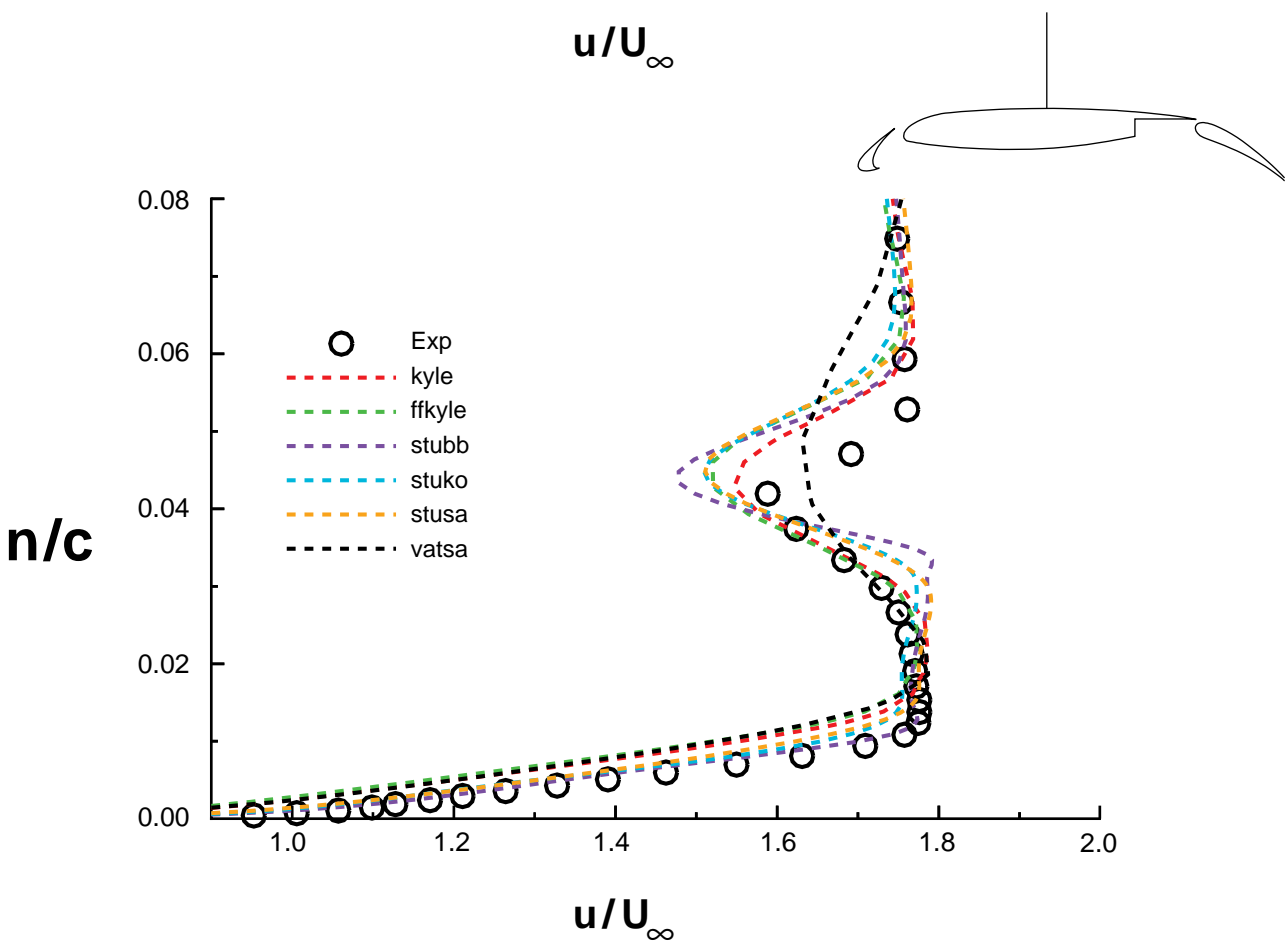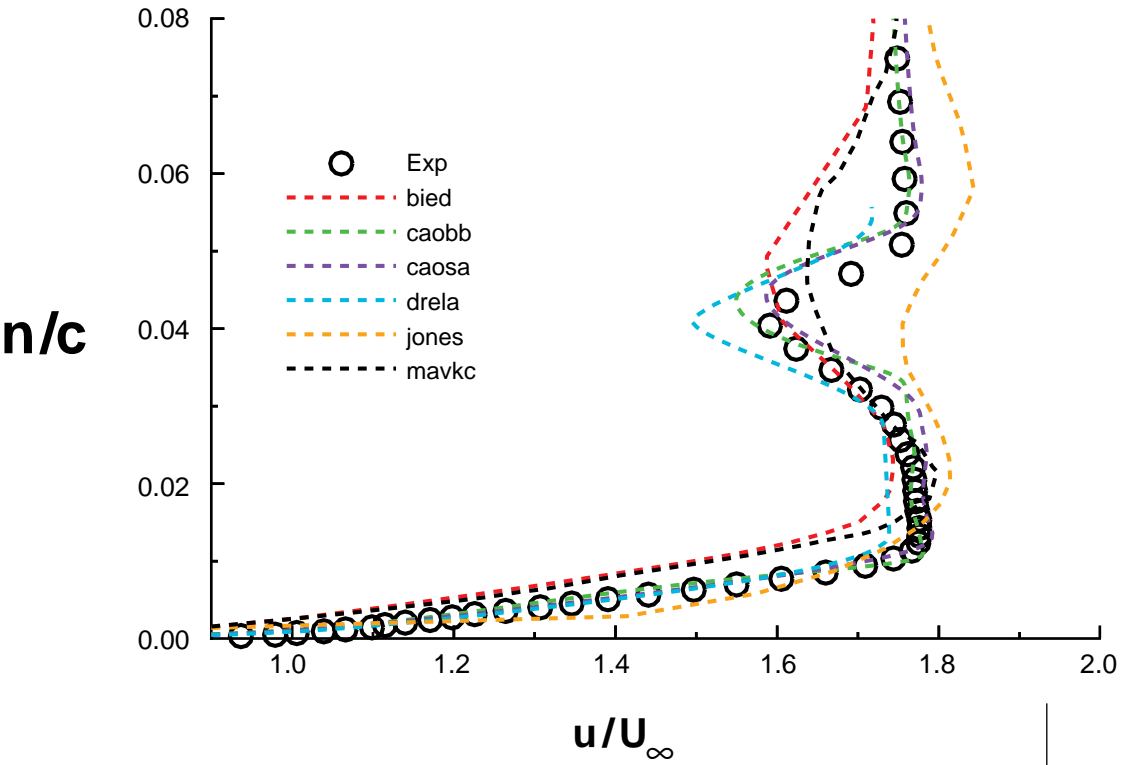
Figure 28. Velocity profiles on the main element -- Geometry A
(x/c=.45, α=21.29°, Re=5 million)

Figure 29. Velocity profiles on the flap -- Geometry A
(x/c=.898, α=21.29°, Re=5 million)

Figure 30. Velocity profiles on the flap -- Geometry A
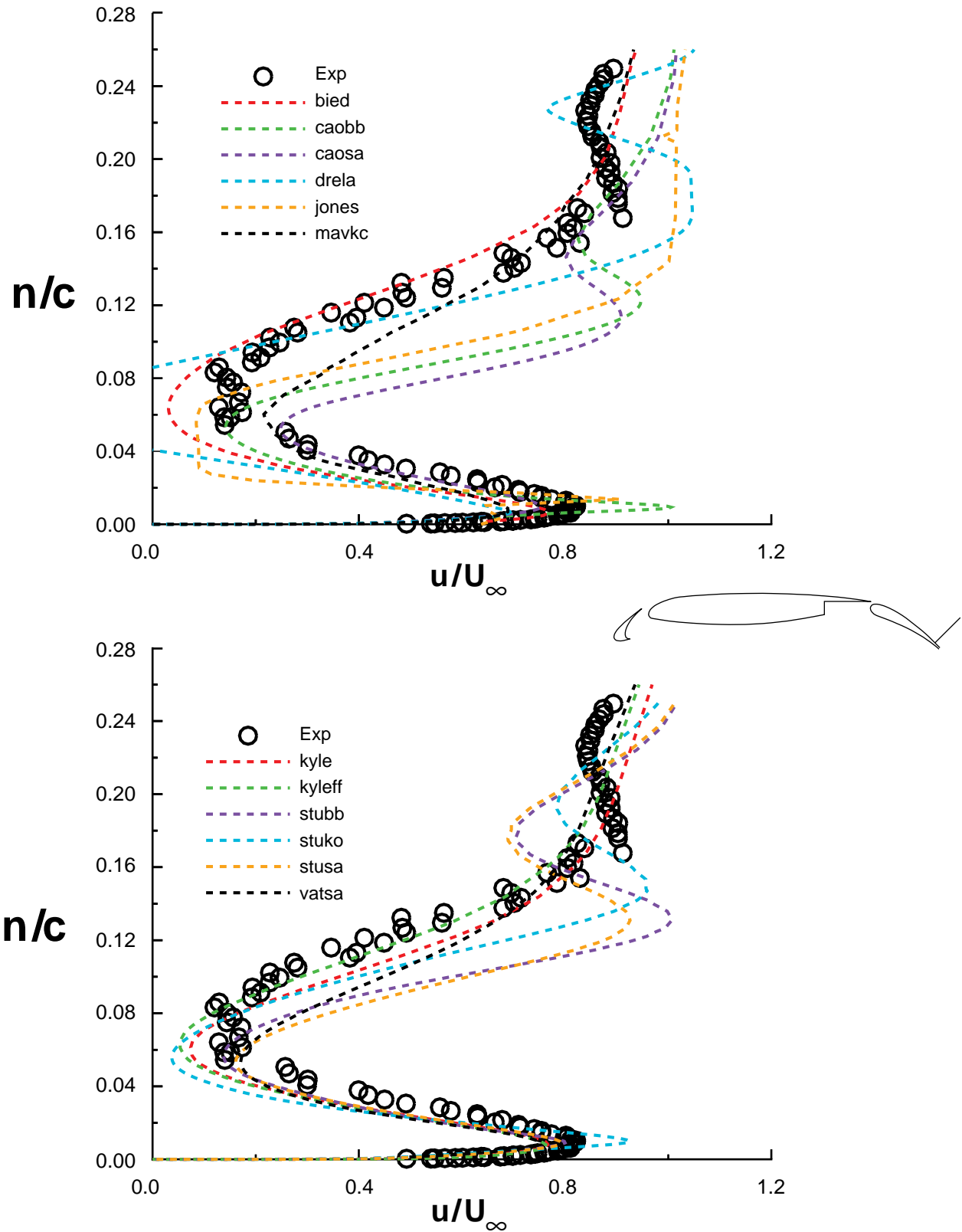(x/c=1.032, α=21.29°, Re=5 million)

Figure 31. Velocity profiles on the flap -- Geometry A
(x/c=1.112, α=21.29°, Re=5 million)